remote sensing

MDPI

Article

Distribution and Degradation Processes of Isolated Permafrost near Buried Oil Pipelines by Means of Electrical Resistivity Tomography and Ground Temperature Monitoring: A Case Study of Da Xing'anling Mountains, Northeast China

Gang Wu [1,2,3], Guoyu Li [1,3,4,*], Yapeng Cao [1,3], Dun Chen [1,3], Shunshun Qi [1,2,3], Fei Wang [5], Kai Gao [1,2,3], Qingsong Du [1,2,3], Xinbin Wang [1], Hongyuan Jing [6] and Zhenrong Zhang [7]

1 State Key Laboratory of Frozen Soil Engineering, Northwest Institute of Eco-Environment and Resources, Chinese Academy of Sciences, Lanzhou 730000, China
2 School of Engineering Science, University of Chinese Academy of Sciences, Beijing 100049, China
3 Da Xing'anling Observation and Research Station of Frozen-Ground Engineering and Environment, Northwest Institute of Eco-Environment and Resources, Chinese Academy of Sciences, Daxing'anling 165000, China
4 College of Architecture and Civil Engineering, Xi'an University of Science and Technology, Xi'an 710054, China
5 Faculty of Civil Engineering and Mechanics, Jiangsu University, Zhenjiang 212013, China
6 PipeChina North Pipeline Company, Langfang 065008, China
7 Daqing (Jiagedaqi) Oil Gas Transportation Branch, PipeChina North Pipeline Company, Jiagedaqi 165000, China
* Correspondence: guoyuli@lzb.ac.cn

Abstract: Human engineering activities and climate warming induce permafrost degradation in the Da Xing'anling Mountains, which may affect the distribution of permafrost and the safety of infrastructure. This study uses the electrical resistivity tomography method, in combination with field surveys and ground temperature monitoring, to investigate the distribution and degradation characteristics of permafrost and influencing factors at a typical monitoring site (MDS304) near the China-Russia Crude Oil Pipeline (CRCOP). The results show that the isolated permafrost in this area is vulnerable to further degradation because of warm oil pipelines and thermal erosion of rivers and ponds. The isolated permafrost is degrading in three directions at the MDS304 site. Specifically, the boundary between permafrost and talik is on both sides of the CRCOP, and permafrost is distributed as islands along a cross-section with a length of about 58–60 m. At present, the vertical hydrothermal influence range of the CRCOP increased to about 10–12 m. The active layer thickness has increased at a rate of 2.0 m/a from about 2.4–6.8 m to 2.5–10.8 m from 2019 to 2021 along this cross-section. Permafrost degradation on the side of the CRCOP's second line is more visible due to the river's lateral thermal erosion, where the talik boundary has moved eastward about 12 m during 2018–2022 at a rate of 3.0 m/a. It is 2.25 times the westward moving speed of the talik boundary on one side of the CRCOP's first line. In contrast, the talik boundary between the CRCOP's first line and the G111 highway also moves westward by about 4 m in 2019–2022. Moreover, the maximum displacement of the CRCOP's second line caused by the thawing of frozen soil has reached up to 1.78 m. The degradation of permafrost may threaten the long-term stability of the pipeline. Moreover, the research results can provide a useful reference for decision-makers to reduce the risk of pipeline freeze-thaw hazards.

Keywords: electrical resistivity tomography; permafrost monitoring; permafrost degradation; climate warming; permafrost and talik distribution; geophysical methods

Citation: Wu, G.; Li, G.; Cao, Y.; Chen, D.; Qi, S.; Wang, F.; Gao, K.; Du, Q.; Wang, X.; Jing, H.; et al. Distribution and Degradation Processes of Isolated Permafrost near Buried Oil Pipelines by Means of Electrical Resistivity Tomography and Ground Temperature Monitoring: A Case Study of Da Xing'anling Mountains, Northeast China. *Remote Sens.* **2023**, *15*, 707. https://doi.org/10.3390/rs15030707

Academic Editor: David Gomez-Ortiz

Received: 20 November 2022
Revised: 27 December 2022
Accepted: 19 January 2023
Published: 25 January 2023

1. Introduction

Global air temperatures are expected to rise by 1–2 °C by the end of this century compared with preindustrial levels [1,2]. Such changes will have serious consequences on the integrity of ecosystems, hydrological systems, and infrastructure. Northeast China

is one of the regions with the most obvious warming trend under the climate warming scenario [3–6]. The northern part of Da Xing'anling Mountains, Northeast China, belongs to the discontinuous permafrost region, and human engineering activities and climate warming seriously threaten the preservation of the permafrost therein [7–10]. In order to ensure the economic development of the Da Xing'anling Mountains, many important infrastructures have also been built in the permafrost region of Northeast China, such as highways, railways, transmission towers, oil and gas pipelines, and other major projects. In order to alleviate the pressure of increasing energy demand, the first and second pipeline projects of the China-Russia Crude Oil Pipeline (CRCOP) in Da Xing'anling Mountains, Northeast China, were completed in 2011 and 2018, respectively. Currently, the CRCOP system of annual transmission capacity is 30 million tons. This pipeline passes through about 441 km of permafrost regions in China. Many buried oil pipelines have been built in permafrost regions around the world, including the Norman Wells pipeline, the Alaska pipeline, the Golmud–Lhasa oil product pipeline, the CRCOP, and others. Engineering damages caused by the freezing and thawing of the foundation soil frequently occur (Figure 1), posing a serious threat to pipeline safety [11–18]. Therefore, to ensure a pipeline's regular operation and minimize the economic loss brought on by pipeline damage, it becomes necessary to monitor the permafrost's thermal state and distribution along the pipeline continuously.

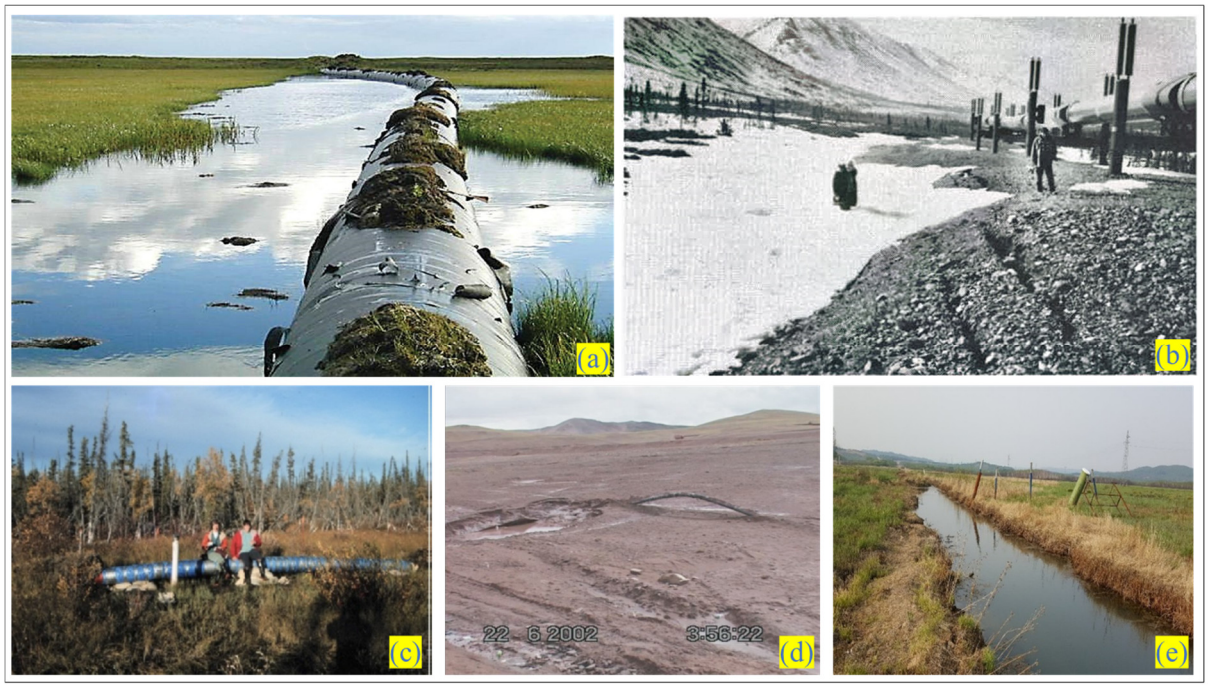

Figure 1. Common oil and gas pipeline damages in permafrost regions. (**a**). The Medveje gas pipeline that once was buried and now is floating in a marsh, resulting partly from the thawing of the permafrost [19]; (**b**). Differential settlement of the workpad in an elevated pipeline segment of the Alaska pipeline [11]; (**c**). Frost heaving of the buried Norman Wells Pipeline in September 1997 [20]; (**d**). Frost heaving and deformation at Wuli of the Product Pipeline from Golmud to Lhasa in June 2002 [20]; (**e**). Surface subsidence occurs in some areas where the CRCOP crosses permafrost regions, resulting in the formation of ponds.

In general, climate conditions and surface ecosystems can be used as a basis for judging whether permafrost exists [21,22]. In the meantime, the spatial distribution of permafrost is also affected by regional micro-topography, hydrological conditions, angle, and direction of the slope, vegetation cover, and fire history [5,23–28]. The comprehensive influence of these factors makes it extremely difficult to judge the distribution of permafrost and

underground ice. Some common exploration methods, such as drilling and pit exploration, have a great influence on the formation and the thermal state of permafrost, which is difficult to recover to its initial state. To ensure the safety of the pipeline system, management personnel strictly restrict the commencement of construction within the scope of management rights, meaning conventional exploration methods are no longer applicable. Electrical resistivity tomography (ERT) technology is convenient, nondestructive, and does not involve excavations, which is based on the principle of measuring the electrical properties of geotechnical materials and hence has been widely used in permafrost research. Moisture content, pore structure, soil texture, temperature, and whether pore water is frozen all influence a geotechnical material's resistivity [29,30]. The resistivity value of ice-rich permafrost is typically 10–100 times higher than that of unfrozen or water-rich soil. The resistivity distribution of strata can be obtained by ERT inversion, and the boundary between permafrost and melting zone can be distinguished according to an abrupt change of resistivity [31,32]. ERT has proven to be extremely effective in identifying and mapping permafrost in discontinuous permafrost in the Yukon, Canada [33]; in permafrost regions in Alaska's plains [34]; in discontinuous permafrost in a thermokarst lake on the Qinghai-Tibet plateau [35]; and in the alpine permafrost region in the Mont Blanc Massif [36]; and in Da Xing'anling Mountains, Northeast China [37].

Currently, ground temperature measurements are often used in conjunction with ERT results as an auxiliary verification method, but it is rare to use multiple ground temperature boreholes to form cross-sectional isotherm profiles combined with ERT results to analyze the distribution and variation of permafrost. Meantime, there have been very few studies that have focused on the distribution and evolution of permafrost and talik under the influence of human engineering activities, such as pipelines and highways in Northeast China. Therefore, we chose the MDS304 site as our study area. The ecological environment in this area is fragile, engineering activities are frequent, and geologic hazards induced by permafrost degradation frequently occur [7,18,38]. The specific objectives of this study are: (1) to draw the distribution map of permafrost and talik of the site using ERT and cross-sectional ground temperature data and (2) to analyze the ground temperature distribution of Jinsong town near the CRCOP, the changes in the active layer, ascertain the evolution process of the permafrost and talik and assess the impact of engineering activities and other factors on permafrost. This study will be beneficial in evaluating the thermal stability of buried pipelines in permafrost regions and reduce the risk of pipeline freeze-thaw hazards.

2. Study Region

The monitoring site is located in Jinsong Town, Da Xing'anling Mountains, Northeast China (124.19° E, 51.16° N). The study area is located on the alluvial plain between the two mountains. The distance between the foot of the mountain is about 1–2 km. Forests, rivers, pipelines, the G111 highway, Fuyu-Xilinji Railway, shrubs, and other landscapes are distributed between the two mountains from west to east. The CRCOP is made up of two buried oil pipelines with a spacing of approximately 12.2 m and an initially buried depth of 2.0 m that operate at a positive temperature all year. The pipeline is about 70 m from the G111 highway. The altitude of this area is about 502 m. The CRCOP traverses to Daqing via Mohe, Tahe, Jiagedaqi, and other locations. It passes through 441 km of permafrost, including 119 km of high-temperature and ice-rich permafrost. This type of permafrost is prone to degradation under climate warming and thermal disturbance caused by engineering activities. We named this site MDS304 because it is 304 km away from the first pump station (Mohe station). As reported by Jin et al. [39], the permafrost area along the CRCOP route can be divided into four types: extensive and discontinuous permafrost (Mohe to Walagan), intermediate discontinuous, with extensive talik (Walagan to Jinsong), sporadic and discontinuous (Jinsong to Jiagedaqi), and isolated patches (Jiagedaqi to Wu'erqi) (Figure 2). This site is located near the boundary between an intermediate discontinuous permafrost zone and a sporadic discontinuous permafrost zone. The marshes here contain more peat and ice-rich permafrost. In order to ensure the

long-term safe operation of the pipeline, insulation and replacement measures are carried out. The insulation material is 8 cm thick rigid polyurethane foam, and polyethylene resin is used as a waterproof shell around the pipeline [18,40–42].

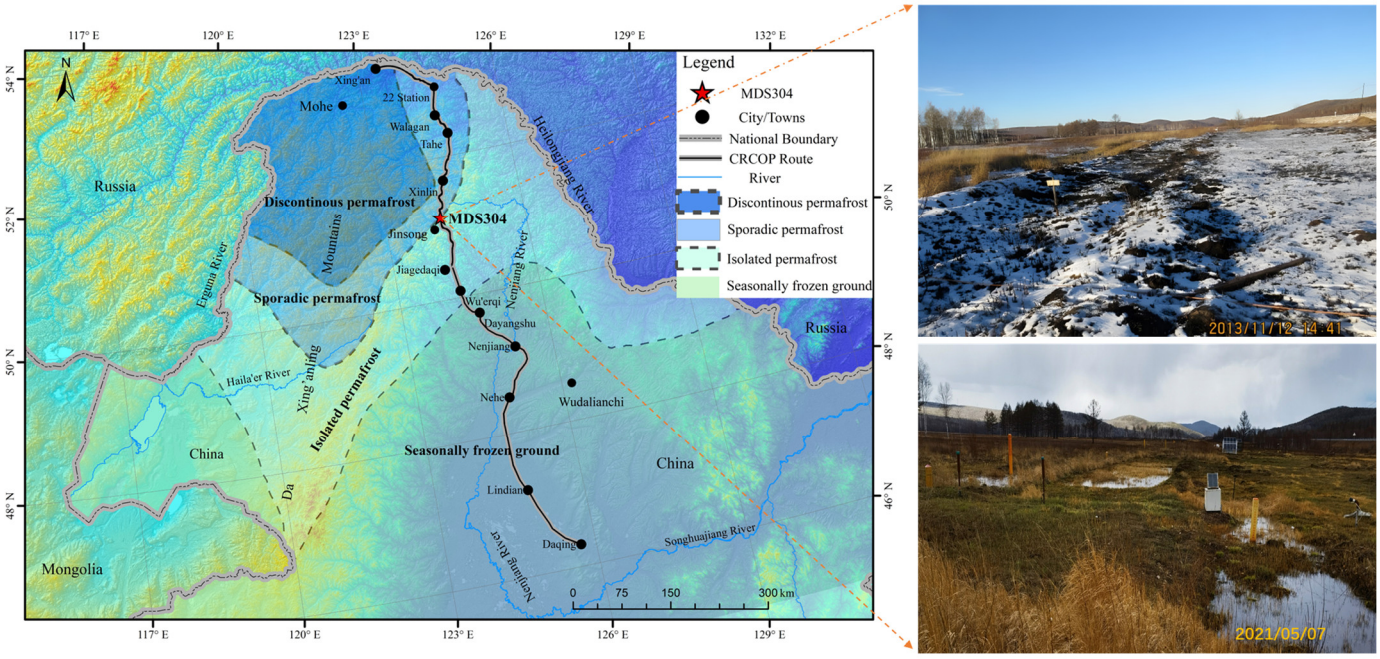

Figure 2. A schematic diagram of the location of the monitoring site, MDS304, and photos were taken in the same location in 2013 and 2021 [38,39,43].

The climate of this region is influenced by alternating high and low-pressure systems, as well as by monsoons in inland and offshore areas. It has a long and dry winter with severe cold and a short, hot, and humid summer with a low mean air temperature and a wide annual range. Its climate can be classified as continental monsoon [44]. Northeast China's permafrost area has shrunk significantly since the 1960s, and the annual average ground temperature has risen [3,6,9,10,44,45]. According to monitoring data obtained at Xinlin and Jiagedaqi station of the National Meteorological Observatory (1972–2020) (http://data.cma.cn/, accessed on 9 December 2021), as shown in Table 1 and Figure 3. The data show that the mean annual precipitation in the study area from 1972 to 2020 was 533.5–540.4 mm, the mean annual air temperature (MAAT) is −2.5 to −0.4 °C, and the annual average temperature of rising linear rate in the Xinlin area is 0.321 °C per decade, while that in Jiagedaqi area is 0.411 °C per decade. This indicates that the trend of climate warming in these two regions is also very clear, and the mean annual precipitation has increased significantly in the last 20 years.

Table 1. Air temperature and precipitation data at Xinlin and Jiagedaqi Meteorological Station along the CRCOP route in permafrost zones from 1972 to 2020.

Station	MAAT (°C)	MjanAT (°C)	MjulAT (°C)	EAT (°C)	MAP (mm)
Xinlin	−2.5	−25.5	18.2	−46.9/37.9	533.5
Jiagedaqi	−0.4	−22.6	19.5	−27.8/22.5	540.4

Note: MAAT: Mean annual air temperature; EAT: Extreme air temperatures; MJulAT: Mean July air temperature; MJanAT: Mean January air temperature; MAP: Mean annual precipitation.

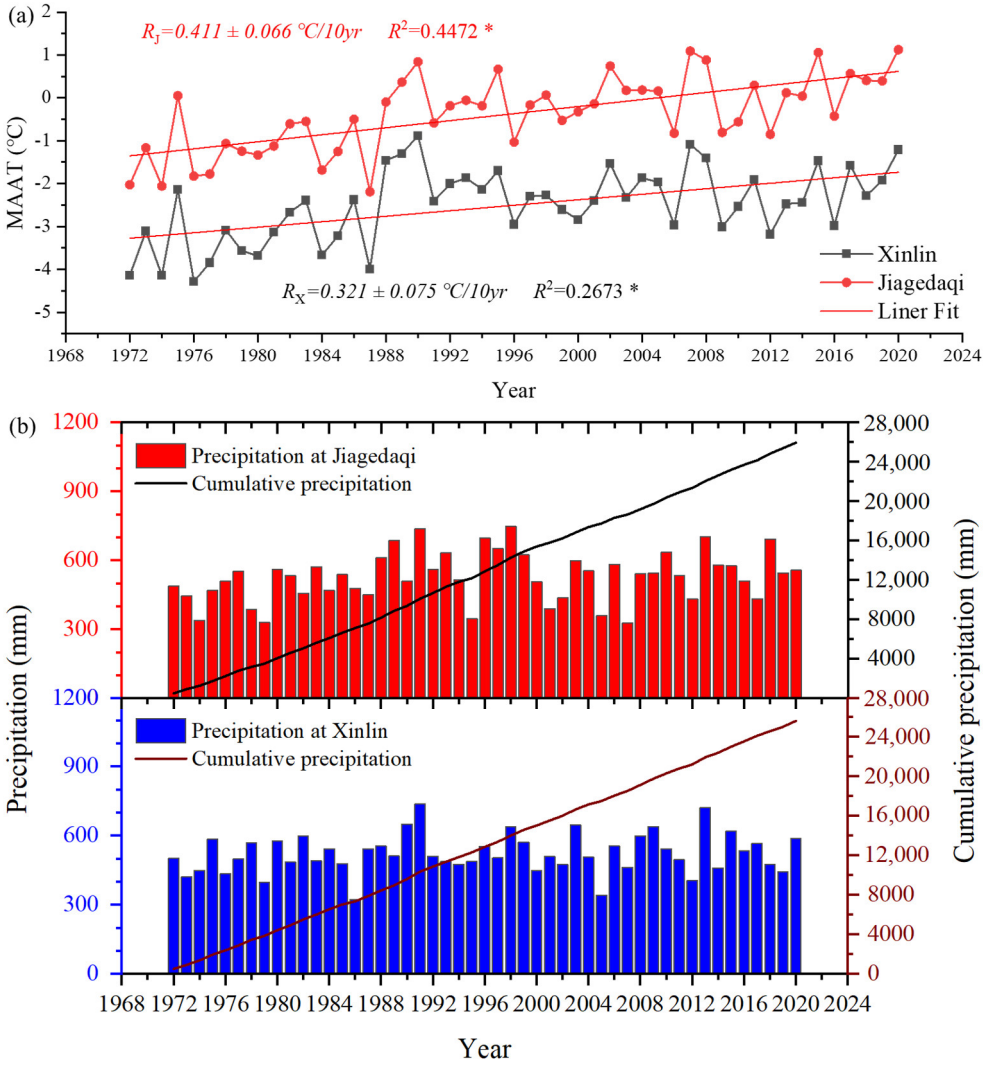

Figure 3. Variations of the (**a**) MAAT and (**b**) annual precipitation at the Xinlin and Jiagedaqi meteorological stations along the CRCOP in the northern Da Xing'anling Mountains, Northeast China, 1972–2020. R_i: Rising rate, (i = J, X); J represents Jiagedaqi; X represents Xinlin station.

Long-term snow cover and dense vegetation cover in the cold season provide favorable conditions for the development and occurrence of permafrost [46,47]. Generally, the soil begins to thaw in April or May and freezes in October or November. The ground surface is usually covered with snow from November to March, and the freezing time lasts about 5 or 6 months per year [7,44,48]. A variety of vegetation is distributed within the pipeline right-of-way, which begins to grow at the end of April and gradually flourishes from May to June. The vegetation is mainly composed of mud sedges and small shrubs, such as rosemary willow and shrub birch (Betula humilis). The forest about 300 m west of the pipeline consists of Larix gmelinii, Pinus pumila, and birch shrubs [49], as shown in Figure 4. However, permafrost in this area is currently suffering from degradation. Figure 4a shows an image of surface vegetation after burning. Runoff recharge in this area mainly comes from rainfall and snow melting. The depth of the groundwater level is about 1.7–3 m. When there is more rainfall, large surface runoff occurs in low-lying areas, resulting in occasional floods and waterlogging (Figure 4b,c). The duration of submersion at the site varies greatly between years, and floods have a significant impact on the underlying permafrost ground temperature [38,39].

Figure 4. Seasonal landscape near the MDS304 site in Jinsong Town: (**a**) After the fire has removed the surface vegetation, the bare surface can still be seen in the spring (18 April 2021); (**b**) Apparent surface subsidence and stagnant water within the pipeline right-of-way (7 May 2021); (**c**) Occasional floods in summer cover the entire valley (17 June 2021); (**d**) Typical wetland type vegetation can be seen on the surface in summer (14 August 2020); (**e**) Less vegetation after the fire and thick snow can be seen in winter (31 October 2019); (**f**) Thicker snow cover on roads and slopes in winter (31 October 2019).

3. Data and Methods

3.1. Geological Information

According to several geotechnical engineering surveys conducted between 2011 and 2018, we obtained geological information about the site through drilling [41], as shown in Figure 5. The intermountain basin's common peat soil is distributed from the surface to 0.8 m and contains many plant roots. The gray silty clay is distributed at a depth of 0.8–2.0 m and contains a small number of fine sand particles. Ice particles and a thin layer of ice can be seen with the naked eye. Below, a 3.5 m thick yellowish-brown gravel sand layer with many ice lenses is distributed, and most of the ice lenses are between 10 and 50 mm thick. Completely weathered granite and strongly weathered granite are distributed from top to bottom in the range of 5.5 to 15 m, and the degree of weathering is gradually weakened. Colors range from gray to yellow-brown to gray-white. These detailed geological data provide essential basic information for ERT investigations regarding the distributions of isolated permafrost and talik [50].

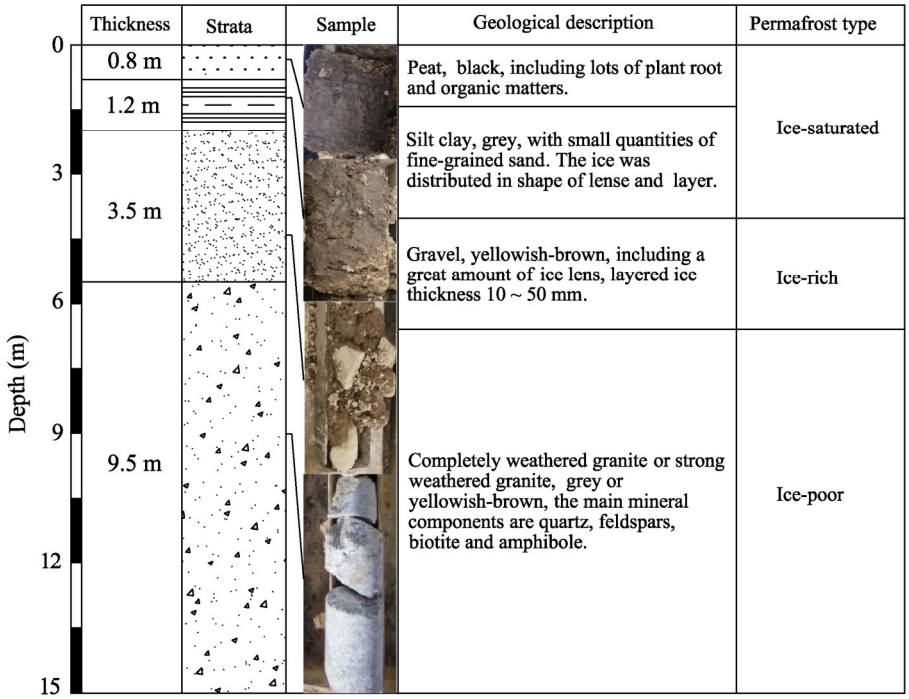

Figure 5. Geological characteristics of the MDS304 site, 0–15 m [42].

3.2. Ground Temperature Monitoring

To obtain the influence of the pipeline operation on the thermal state of permafrost, Chang et al. [40] and Li et al. [42,51] drilled several ground temperature monitoring boreholes at the site and utilized thermistor chains to measure the soil temperature at different depths, shown in Figure 6 as Profile 1. The thermistor chain was manufactured by the State Key Laboratory of Permafrost Engineering, and its sensitivity is 0.05 °C. The thermistor chain is linked by a CR3000 data logger, and data are collected by a field data acquisition system equipped with solar panels and a remote data transmission module. Because of the poor local communication signal conditions, data acquisition in some cases necessitates researchers reading on-site. Figure 6 depicts a schematic diagram of the field monitoring system as well as the layout of the ground temperature boreholes. Table 2 depicts the thermistor arrangement in depth. Figure 6 shows the previous ground temperature boreholes as the red icon Ti' (i = 1, 2, 3, 4, 5, 6). As a result of being frozen and pulled up, some of the steel tubes were damaged. After September 2017, only borehole T5′ remained, which was renamed T4 when a new thermistor chain was installed. Previous ground temperature data show that the ground temperature of the T3 borehole was positive (it was previously used as a control borehole), making monitoring changes in permafrost impossible. As a result, in December 2018, borehole T6 was built about 25 m deep near the CRCOP's first line as a new control borehole for ground temperature monitoring. At the same time, a T7 borehole with a depth of 20 m is added near the foot of the highway slope [42,43].

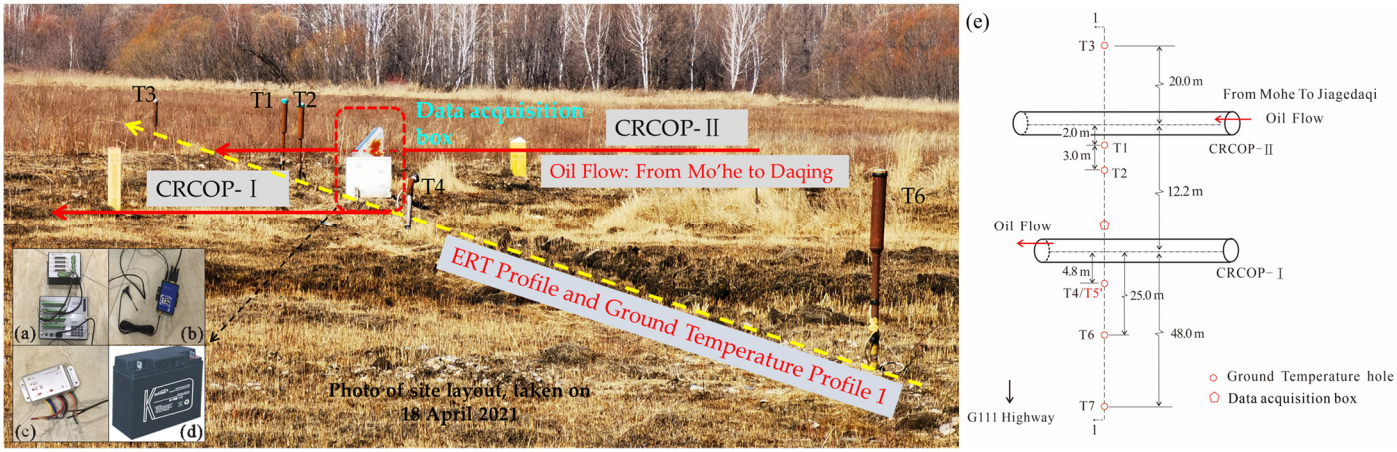

Figure 6. Diagram for the ground temperature monitoring system at the MDS304 site (**e**), ground temperatures are measured using thermistor chains connected to a CR3000 data logger: (**a**) CR3000 data logger with a TRM128 multiplexer, (**b**) Wireless transmission module (HKT-DTU, Campbell Scientific, Inc., Logan, Utah, USA), (**c**) solar charge controller (Phocos ECO (10 A), UIm, Germany), and (**d**) battery cell [51]. The photo was taken on 18 April 2021. Note: T1, . . . , T7 is a ground temperature borehole; CRCOP-I: the CRCOP's first line; CRCOP-II: the CRCOP's second line.

Table 2. Ground temperature monitoring information of boreholes near the CROCP at the MDS304 site for Profile 1, from 2011 to 2022.

The Distance from Borehole T3 (m)	Borehole	Monitoring Depth (m)	Measuring Internal	Working Period
0	T3	0.3, −0.2, −0.7, −1.2, −1.7, −2.2, −2.7, −3.2, −3.7, −4.7, −5.7, −6.7, −7.7, −8.7, −9.7, −10.7, −11.7, −12.7, −13.7, −14.7, −15.7, −16.7, −17.7, −18.7, −19.7	25, 2 h, Auto	October 2017–Now
22	T1	0, −0.5, −1, −1.5, −2, −2.5, −3, −3.5, −4, −5, −6, −7, −8, −9, −10, −11, −12, −13, −14, −15, −16, −17, −18, −19, −20	25, 2 h, Auto	October 2017–Now
25	T2	0, −0.5, −1, −1.5, −2, −2.5, −3, −3.5, −4, −5, −6, −7, −8, −9, −10, −11, −12, −13, −14, −15, −16, −17, −18, −19, −20	25, 2 h, Auto	October 2017–Now
37	T4	0.1, −0.4, −0.9, −1.4, −1.9, −2.4, −2.9, −3.4, −3.9, −4.9, −5.9, −6.9, −7.9, −8.9, −9.9, −10.9, −11.9, −12.9, −13.9, −14.9	20, 2 h, Auto	November 2011–Now
57	T6	0, −0.5, −1, −1.5, −2, −2.5, −3, −4, −5, −6, −7, −8, −9, −10, −11, −12, −13, −14, −15, −16, −17, −18, −19, −20	24, 2 h, Auto	December 2018–Now
80	T7	0, −0.5, −1, −1.5, −2, −2.5, −3, −4, −5, −6, −7, −8, −9, −10, −11, −12, −13, −14, −15, −16, −17, −18, −19, −20	24, 2 h, Auto	December 2018–Now

3.3. Oil Temperature Acquisition

The warm oil pipeline transmits a lot of heat to the permafrost, which greatly affects the thermal state of the permafrost around the pipeline. According to the investigation report by Li et al. [18], several freeze-thaw hazards, including ice cones, frost heave mounds, and pipeline trench settlements, have emerged along the pipeline. These damages posed a major threat to pipeline safety. Meantime, temperature losses occur during the transit of crude oil, which requires the pump station to pressurize and heat the oil. As a result, it is critical to understand the variations in oil temperature at pumping stations along the pipeline and take the necessary precautions to prevent the excessive growth of any melt rings around the pipeline in time to preserve the pipeline's normal operation. It is extremely

difficult to directly monitor the temperature of crude oil in the pipeline at the MDS304 site. According to the design oil temperature when entering the first pump station (Mohe station), Li et al. [52] used a quasi-three-dimensional transient heat transfer model to predict the oil temperature distribution of the entire line. So, we use pump station oil temperature interpolation to obtain the temperature of the pipeline at a certain location. It mainly ignores the heat exchange between oil and permafrost and the influence of oil temperature rise caused by oil-pipe friction during oil transportation. The authors monitored the oil temperature at three oil pumping stations in the permafrost zone on a continual basis (at the Mohe, Tahe, and Jigedaqi oil pump stations, in order from north to south). Since the pipeline's initial operation, we have collected monthly average oil temperature data from 2011 to 2020. The oil temperature variation law in the actual operation of the CRCOP's first line is given in Section 4.1.

3.4. Electrical Resistivity Tomography

In order to reduce surface disturbances and to analyze the thermal condition and distribution of frozen soil around the pipeline efficiently, we have conducted ERT tests along the monitoring site for many years. We use the Advanced Geosciences Incorporated (Austin, TX, USA) SuperSting R8 Polarization Meter to measure resistivity (Figure 7b). The electrode spacing of 2.0 m or 2.5 m is chosen depending on the number of available electrodes and the depth of the target formation to achieve a maximum penetration depth of at least 20 m and a section measurement length of about 100–120 m. Many researchers have achieved good results in identifying and mapping the distribution range of permafrost or talik by using Wenner or Wenner-Schlumberger array because it has the best signal-to-noise ratio [33,35,53]. As a result, the Wenner-Schlumberger electrode array has been employed in this study. Because the freezing depth of strata often reaches its maximum in April due to the lag effect of air temperature on ground temperature [54], we conduct ERT tests at the Jinsong town MDS304 site every spring. There is a thick peat soil layer and plant roots on the surface, and thermal conductivity is low, which can slow permafrost melting, so there is often ice on the site's surface in early spring. Therefore, when placing the electrode in the soil layer, it is necessary to make the electrode in good contact with the soil layer as far as possible, and the appropriate depth is 30–40 cm. When the resistivity exceeds the allowable range of 0–10,000 Ω·m, salt water is added to the vicinity of the electrode device until the resistivity falls within the allowable range before the ERT test. We successfully obtained ERT test results in 2018, 2019, and 2021, and Figure 7 showed our working photos from when we conducted ERT tests at the MDS304 site in April 2021 and a front view of the site layout.

When obtaining ERT test data, human errors are unavoidable. The accuracy of the ERT data collection and interpretation is determined by the researchers' experience and professional level, as well as the type of electrode array used and the selection of the ERT inversion parameters [50,53]. Furthermore, surface water and local high-resistivity geological bodies (thicker underground ice) have an impact on the accuracy of ERT test results [55]. We decided to exclude several measurements based on different criteria, namely, the effective electric current, the voltage, the standard deviation between reciprocal measures, and the presence of outliers considering the values of a single measurement in comparison with surrounding ones in the time series. Data inversion is accomplished using EarthImager 2D software (Version: 2.4.0, Advanced Geosciences, Inc., Austin, Texas, USA). Meantime, the accuracy of inverted measured data is related to many factors, including the choice of the inversion parameters, such as the damping coefficient, smooth filter coefficient, number of iterations, and so on [56–60]. In order to reduce the influence of noise, the Marquardt and Occam combined inversion method and a robust constraint (L1 norm) on the model resistivity are used to obtain an inversion result with a global root mean square (RMS) error of less than 5% [61].

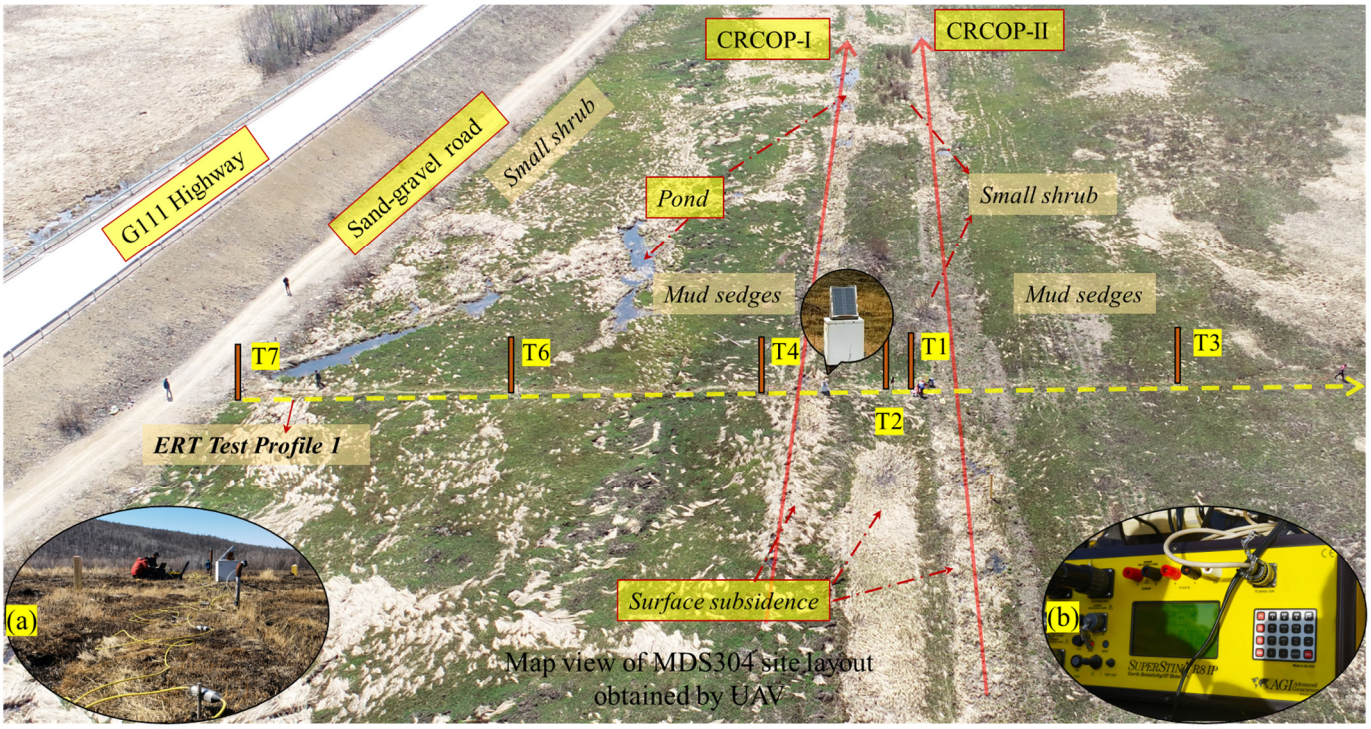

Figure 7. Researchers using the SuperSting R8 Polarization Meter to conduct ERT tests at the MDS304 site in Jinsong town on 18 April 2021 (**a**), and photo of SuperSting R8 Polarization Meter (**b**). This map view image was captured by UVA on 19 May 2022. Note: T1, . . . , T7 is a ground temperature borehole; CRCOP-I: the CRCOP's first line; CRCOP-II: the CRCOP's second line.

4. Results

4.1. Characteristics of the CRCOP's Oil Temperature Variation

Figure 8 displays the monthly average oil temperature variations of the permafrost zones at the Mohe, Tahe, and Jiagedaqi pump stations along the CRCOP's first line between 2011 and 2020. The monitoring results show that the CRCOP system operates year-round at the temperature of 6.03–27.74 °C in 2020, which is much higher than the design oil temperature (−6.4 to 3.7 °C) [37,41,62]. The oil temperature monitoring results show that the monthly average oil temperature of these three pumping stations is warming obviously with the increase in running time. Especially after 2017, this trend is more obvious.

The characteristic values (monthly minimum, monthly maximum, monthly average) of the Mohe, Tahe, and Jiagedaqi pumping stations' inlet and outlet oil temperatures in 2012, 2018, and 2020 are shown in Table 3. We used the monthly average oil temperature as an example to analyze the change in oil temperature over an eight-year period (2012–2020). Mohe station's inlet and outlet monthly average oil temperature climbed by 18.06 °C and 15.68 °C, respectively, from 2012 to 2020, and the rising rates were 2.26 °C/a and 1.96 °C/a, respectively; those at Tahe station climbed by 8.5 °C and 9.99 °C, respectively, with rising rates of 1.06 °C/a and 1.25 °C/a; and those at Jiagedaqi station increased by 4.49 °C, 4.41 °C, respectively, with rising rates of 0.56 °C/a, 0.55 °C/a, respectively. The results show that the farther the distance from the Mohe station, the lower the heating rate of the oil temperature at the respective pumping station. The outlet oil temperature is frequently greater than the inlet oil temperature after the crude oil has been pressured by a pump station. In 2020, the Mohe station's outlet monthly average oil temperature was 0.8 to 1.5 °C warmer than that of the inlet (it rose by 1.81 to 3.52 °C in 2012). With an increase in the distance from the pipeline to Mohe station, the oil temperature of the pumping stations of Tahe and Jiagedaqi decreased in turn. From Mohe Station to Jiagedaqi Station, the outlet's monthly average oil temperature dropped by 13.71 °C in 2020, a 58% decrease.

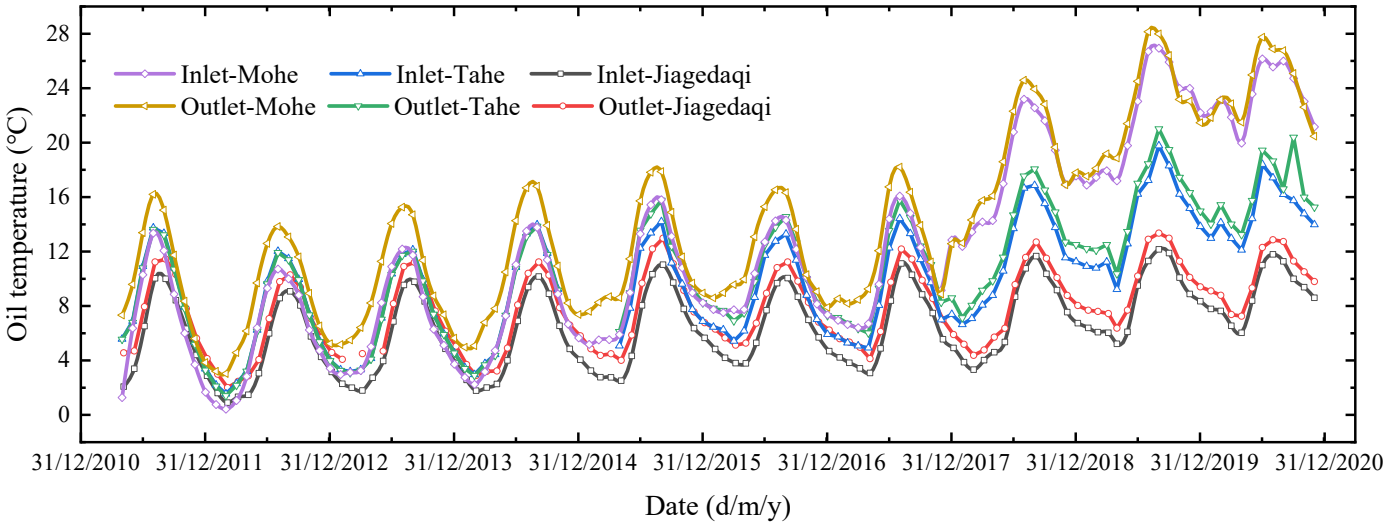

Figure 8. Monthly average inlet and outlet oil temperatures of the Mohe, Tahe, and Jiagedaqi pumping stations (2011–2020) of the CRCOP's first line.

Table 3. Characteristic values of the Mohe, Tahe, and Jiagedaqi pumping stations' monthly average inlet and outlet oil temperatures, 2012, 2018, and 2020.

Pump Station	The Distance to Mohe Station	Monthly Average Oil Temperature	2012			2018			2020		
			Min	Max	Average	Min	Max	Average	Min	Max	Average
Mohe	0 km	Inlet	0.42	10.71	5.24	12.38	23.19	17.39	19.96	26.15	23.30
		Outlet	3.04	13.84	8.09	12.58	24.58	18.35	20.47	27.74	23.78
Tahe	156.5 km	Inlet	1.55	12.03	6.25	6.64	16.86	11.38	12.11	18.41	14.75
		Outlet	1.41	11.92	6.16	7.13	18.06	12.39	13.24	20.39	16.15
Jiagedaqi	390 km	Inlet	0.90	9.07	4.41	3.33	11.66	7.02	6.03	11.79	8.90
		Outlet	2.01	10.28	5.65	4.38	12.70	8.04	7.25	12.86	10.06

As we all know, it is a challenging task to accurately predict the oil temperature at a certain location in buried pipelines in permafrost regions. The temperature of crude oil in operation is affected by factors such as pipeline buried depth, ground temperature and water content of permafrost, and whether the insulation layer is set, outlet oil temperature, crude oil quality, flow rate, and friction heat generation between pipeline and oil during transportation [52]. Therefore, it is assumed here that the oil temperature is in an ideal linear decreasing state during transportation. The temperature reduction range of the oil within approximately 233.5 km between Tahe and Jiagedaqi stations was calculated using data from Tahe station's outlet oil temperature ($T_{\mathrm{Ta\_o}}$) and Jiagedaqi station's inlet oil temperature ($T_{\mathrm{Jia\_I}}$). Using a simplified linear model (Equation (1)) of oil temperature loss in the oil transportation process, the oil temperature at the MDS304 site ($T_{\mathrm{oil\ in\ MDS304}}$) in 2020 was calculated to range from 8.64 to 14.27 °C, with an average of 11.52 °C.

$$T_{\mathrm{oil\ in\ MDS304}} = T_{\mathrm{Ta\_o}} - \frac{L_{(\mathrm{Tahe-MDS304})}}{L_{(\mathrm{Tahe-Jiagedaqi})}} \times (T_{\mathrm{Ta\_o}} - T_{\mathrm{Jia\_I}}) \quad (1)$$

where L is the distance, $L_{(\mathrm{Tahe-Jiagedaqi})}$ is the distance between Tahe station and Jiagadaq station.

The continuous thermal effect of oil temperature on permafrost increases the radius of the soil melting circle around the pipeline year after year. Even if some sections of the pipeline are insulated, the risk of thawing and sinking of the permafrost foundation beneath the pipeline cannot be avoided [18,38,63]. Monitoring permafrost distribution and ground temperature around the pipeline on a regular basis can provide useful information for developing countermeasures to reduce the risk of pipeline thaw settlement.

4.2. ERT for Permafrost

We used sections perpendicular to the two pipelines to make ERT measurements to ensure that we could analyze the influence range of the pipeline on the frozen soil (Profile 1, Figure 6). On 12 April 2018, ERT was employed to measure the formation resistivity at the MDS304 site. The testing device was positioned between the two pipelines. The measurement length was 120 m, 61 electrodes were employed, and the test electrode distance was 2 m. The ERT inversion profile is shown in Figure 9a. The global RMS error of the inversion result is 3.0%, which shows that the data have high reliability. Figure 9 also shows the pipeline's location as well as the locations of boreholes T3, T1, T2, and T4 and the curve of ground temperature with a depth of boreholes T1 and T3 (Figure 9b). It is well known that the location of the pipeline in the permafrost will change due to thaw subsidence. There was a surface subsidence and a pond about 0.1 m deep and 1 m wide between the two pipelines. It is worth noting that inverse modeling has uncertainty and non-uniqueness. As a result, in the analysis of ERT inversion results, we pay more attention to the area changes of some color block distribution areas. The ground temperature curves of T1 and T3 on 12 April 2018 show that the active layer thickness of the underlying frozen soil of T3 is 3.2 m, while the artificial permafrost table under T1, 2 m away from the CRCOP's second line, is 3.8 m, which is greatly affected by pipeline heat. The position of 0 °C in the ground temperature curve corresponds well with the shallow area of the ERT inversion profile in depth, and the approximate position is about the interface of the yellow-green block. The acquisition method and resolution of the two images are different (Figure 9), and this feature is only used as a reference for the identification of permafrost and talik in the analysis of the ERT inversion profile. The ERT inversion profile revealed a sizable talik area between 5 and 45 m in Figure 9a, as well as a thawed zone surrounding the pipeline, an area indicated by a red dotted line. It was found that the lower the temperature of the frozen soil, the greater the resistivity. A 2–3 m thick frozen layer existed near the surface with a blue or dark blue, where the greater the resistivity of the stratum, the closer it was to the east side. Because the frozen layer that formed near the surface in winter had not yet melted, the permafrost was distributed in the deep part. A thawed interlayer with a low-resistivity zone existed at a depth of about 2.5–4.5 m between 86 and 104 m in Figure 9a, and its length is about 18 m. The resistivity distribution of the melted circle around the pipeline showed that the two pipelines' hydrothermal influence ranges differed. The frozen soil around the pipeline built earlier was obviously more affected by the pipeline's heat, and the depth of the vertical heat influence range was approximately 8–10 m. This may be related to the difference in topography, vegetation type, peat layer thickness, fire history, and engineering disturbance history.

On 6 April 2019, an ERT test was performed at the same section of the MDS304 site. The ERT test was conducted at a polar distance of 2 m, using 61 electrodes and a measuring length of 120 m. The measurement time was about a week earlier than the previous year. Figure 10 shows the ERT inversion profile with an RMS error of 2.7% on 6 April 2019 at the MDS304 site and the curve of ground temperature with a depth of boreholes T1 and T3. The ground temperature curves of T1 and T3 on 6 April 2019 show that the underlying T3 is seasonally frozen soil with an active layer thickness of 3.5 m, while the artificial permafrost table under T1 is 5.4 m, about 1.6m more than that in 2018, and a thawed interlayer about 1.3 m thick is developed. Moreover, there is a high resistance area near T1 (Figure 10a), which may affect the imaging accuracy of ERT equipment for deep formation. Therefore, the results near T1 in the ERT inversion profile are not analyzed here. In Figure 10a, a 2.5–5 m thick frozen layer can be seen near the surface, a blue or dark blue area. The distribution of formation resistivity showed that the ground temperature was lower, closer to the east side. On the west side, there was an obvious melt zone beneath the surface, and there was also a big talik area near borehole T3. We discovered that the hydrothermal influence range near the pipeline tended to expand horizontally, forming a large, interconnected melt zone around the CRCOP when combined with geological data from the site. This could have been caused by increased surface subsidence displacement and surface area of the surface

pond in autumn. Additionally, thermal erosion of the pond thickened the active layer near the pipeline. The freezing depth of the stratum increased noticeably in winter, and the maximum depth was about 5 m, and the surface pond's vertical hydrothermal influence range increased significantly in comparison to 2018.

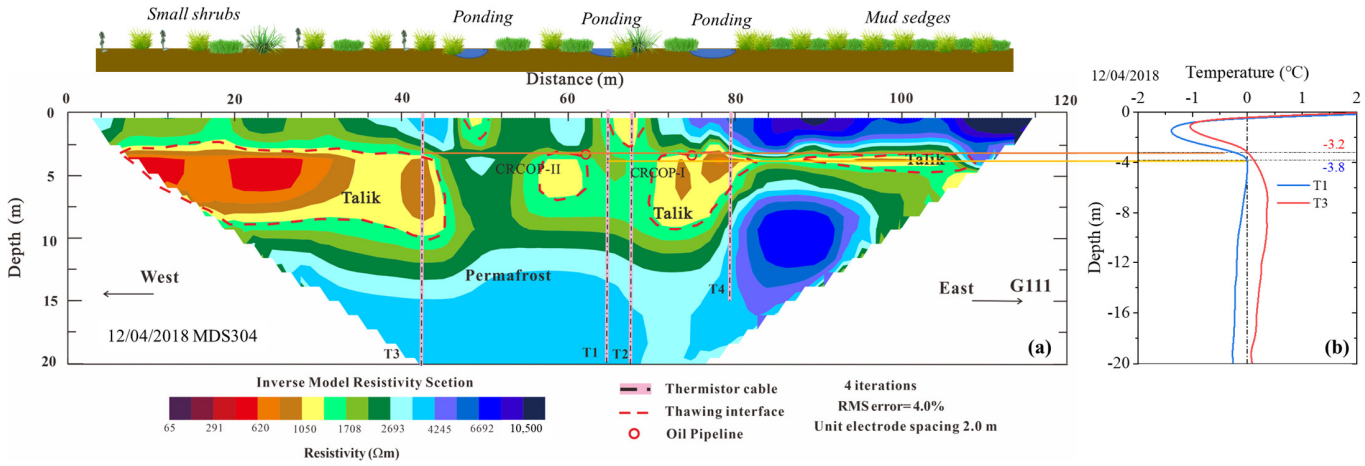

Figure 9. On 12 April 2018, an inversion profile of the ERT test results with an RMS error of 4.0% was obtained at the MDS304 site (Profile 1) (**a**), and the curve of ground temperature with a depth of borehole T1 and T3 (**b**). Note: T1, . . . , T4 is a ground temperature borehole; CRCOP-I: the CRCOP's first line; CRCOP-II: the CRCOP's second line.

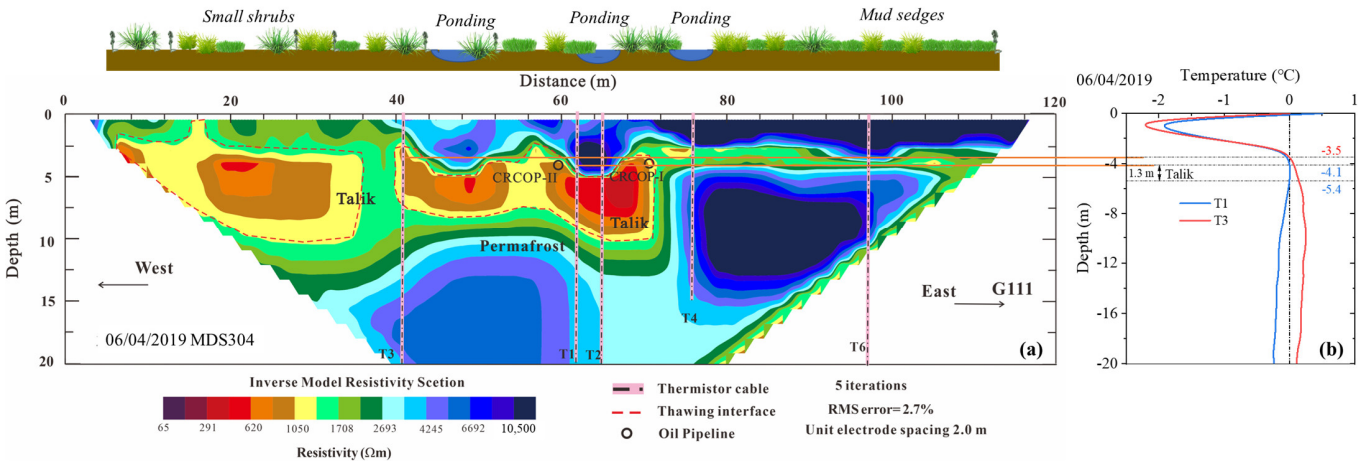

Figure 10. On 6 April 2019, an inversion profile of the ERT test results with an RMS error of 2.7% was obtained at the MDS304 site (Profile 1) (**a**), and the curve of ground temperature with a depth of borehole T1 and T3 (**b**). Note: T1, . . . , T6 is a ground temperature borehole; CRCOP-I: the CRCOP's first line; CRCOP-II: the CRCOP's second line.

Due to the impact of the 2019 coronavirus pandemic, researchers were only able to work at home in April 2020 and were unable to go to the study area to make geophysical measurements. Therefore, the ERT inversion profile with an RMS error of 3.6% recorded on 18 April 2021 at the MDS304 site and the curve of ground temperature with a depth of borehole T1 and T3 are depicted in Figure 11. The ground temperature curves of T1 and T3 from 2018 to 2021 show that the active layer thickness of the underlying seasonal frozen soil of T3 increased from 3.2 m to 4.7 m, while the artificial permafrost table under T1 increased from 3.8 m to 8.3 m, the thickness of thawed interlayer increases to about 5.0 m. This analysis contributes to a better overall understanding of ERT inversion results. The ERT test in 2021 was conducted at a polar distance of 2.5 m, using 40 electrodes and a measuring

length of 100 m. It was found that the size of the pond in the middle of the pipeline increased to about 0.3 m deep, 2.0 m wide, and 4.0 m long. The reason for the formation of a noticeable low-resistivity zone close to borehole T2 was the pond created by surface subsidence in the middle of the pipeline. Taking the T6 hole as a reference (Figure 11a), the thickness and range of the surface frozen layer on 18 April 2021 are significantly smaller than those on 6 April 2019. Compared with the ERT results in 2018 and 2019, the maximum resistivity of the frozen soil or bedrock beneath the surface was approximately 4400 Ω·m lower, but we pay more attention to the area changes of some color block distribution areas. Under the background of a rising oil temperature and an expanded range of ground surface ponds' hydrothermal influence, a common influence area formed near the CRCOP's first line in 2021 between 48 and 76 m in Figure 11a, and the vertical hydrothermal influence range increased to about 10–12 m, and there is little difference between the CRCOP's first and second lines. Taking the T3 hole as a reference (Figure 11a), the area of low resistivity (indicated by the red dotted line) on the west side of the CRCOP's second line decreased year by year from 2018 to 2021. It shows that the ground temperature recovered year by year after the completion of the project of the CRCOP's second line at the end of 2017. However, the melting circle radius of permafrost near the pipeline is still expanding.

In general, the melting radius of the permafrost around the pipeline was expanding year by year, and surface subsidence displacement was also increasing, so we believe the pipeline's buried depth is changing. We have used the RD8000 Locator to detect the pipeline's current specific buried depth in August 2022. According to the results, the buried depth of the top of the CRCOP's first line is approximately 3.22 m, and that of the second line is approximately 3.78 m. Because the pipeline diameter is 813 mm and the buried depth is approximately 3–4.5 m, the ERT test results are in good agreement with the actual situation. Therefore, the maximum displacement of the CRCOP's second line caused by the thawing of frozen soil has reached 1.78 m, and the settlement of the CRCOP's first line is about 1.22 m.

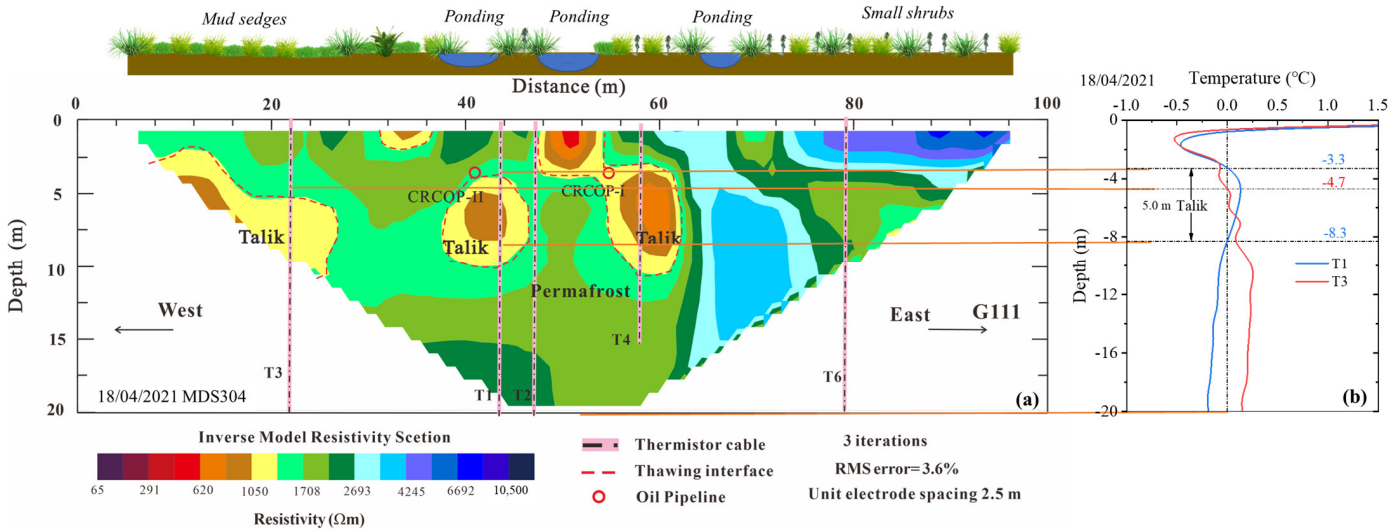

Figure 11. On 18 April 2021, an inversion profile of the ERT test results with an RMS error of 3.6% was obtained at the MDS304 site (Profile 1) (**a**), and the curve of ground temperature with a depth of borehole T1 and T3 (**b**). Note: T1, . . . , T6 is a ground temperature borehole; CRCOP-I: the CRCOP's first line; CRCOP-II: the CRCOP's second line.

4.3. Cross-Sectional Isotherm Profile Showing Isolated Permafrost Distribution

Several ground temperature monitoring boreholes have been installed at the MDS304 site in the Da Xing'anling Mountains since 2011 and are used to monitor the hydrothermal effect range of the CRCOP running with high oil temperatures in permafrost zones. When the CRCOP's first line was constructed in 2011, the 15 m deep T4 borehole was drilled,

while T3, T1, and T2 boreholes with depths of 20 m were added following the completion of the CRCOP's second line in October 2017. The T6 and T7 boreholes, with a depth of 20 m, were added in December 2018. The data from six ground temperature monitoring boreholes on the pipeline's cross section are plotted according to the timings of the ERT tests, and the cross-sectional isothermal profiles at fixed several times were obtained (see Figure 12). The T3, T1, T2, T4, T6, and T7 boreholes correspond to positions of 0 m, 22 m, 25 m, 37 m, 57 m, and 80 m, respectively, in Figure 12. Figure 12 shows the ground temperature distribution of permafrost underlying the pipeline right-of-way from 2018 to 2022 by inverse distance weighting method. The mean annual ground temperature of the isolated permafrost is about −0.25 °C, which fluctuates little, but the permafrost area in the range of −0.25 °C isotherm decreases. Overall, the isolated permafrost near the CRCOP at the MDS304 site is degraded in three directions. From April 2018 to April 2022, the 0 °C isotherm at a depth of 4–6 m below the left surface extends from about 22 m to 34 m, the area of permafrost further shrank, and the moving rate of the talik boundary to the east was about 3.0 m/a, while the talik boundary on the right extended from 64 m to 60 m in the period 2019–2022. Vertically, the depth of the 0 °C line at the left and right ends increased to varying degrees from April 2018 to April 2022, the left side gradually increased from about 3 m to 4.6 m, and the right 0 °C line fluctuated back and forth in the range 2–3 m. From the horizontal point of view, isolated permafrost was distributed underlying the surface between the pipeline and the G111 highway, the area gradually shrunk, and the ground temperature was gradually increasing. Meantime, taking the T1 hole as a reference (Figure 12), the thickness of talik underlying the CRCOP's second line increased from 0 m to about 14 m between April 2018 and April 2022, while it was only about 8.0 m in April 2021. Our field investigation found that there is a perennial river about 3–5 m wide at 200 m west of the pipeline. At the same time, there are longitudinal cracks and ponds formed by uneven surface subsidence near the pipeline. The geological data show that the stratum contains more gravel and sand at a depth of 2–6 m, and the permeability is better. The short-term rapid degradation of isolated permafrost may be related to the continuous lateral thermal erosion of rivers in intermountain valleys. At the same time, this is the result of many factors, including climate warming and rising oil temperature year by year, which comprehensively affect the thermal state of permafrost. Other factors may include the occurrence of perennial stagnant water due to surface subsidence and occasional floods during the rainy season, as well as human engineering activities and forest workers in the Da Xing'anling Mountains using artificially controlled fire to remove surface vegetation cover to create a fire prevention zone every autumn [64–69]. However, the role of these factors in the process of permafrost degradation in this site needs further study.

The active layer reaches a maximum thawing depth in late October. Figure 13 shows the ground temperature distribution of the MDS304 site on 15 October 2019 and 15 October 2021 by inverse distance weighting method. By comparing Figure 13a,b, the active layer thickness below the position of 8 m to 68 m was about 2.4–6.8 m on 15 October 2019. The active layer thickness below the position of 12 m to 68 m was about 2.5–10.8 m on 15 October 2021. This comparison shows that the maximum thickness of the active layer increased by about 4 m in two years under the common thermal influence of the two pipelines, and the cross-sectional distribution length of isolated permafrost near the MDS304 pipeline was about 58–60 m.

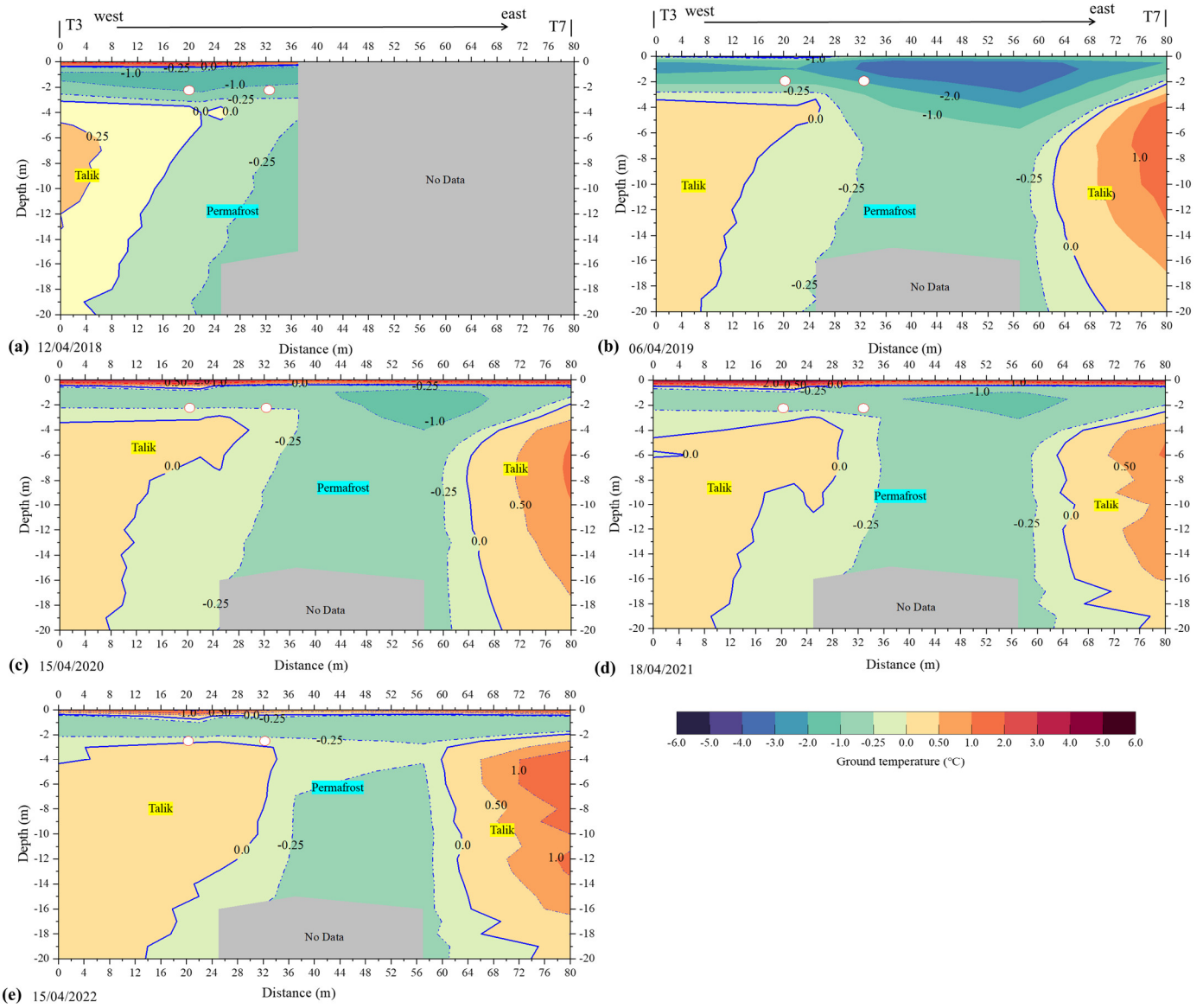

Figure 12. The cross-sectional isotherm profiles of the MDS304 site were drawn using the inverse distance weighting method from mid-April 2018 to mid-April 2022, including the ERT exploration period: (**a**) 12 April 2018, (**b**) 6 April 2019 (**c**) 15 April 2020 (**d**) 18 April 2021 and (**e**) 15 April 2022. Note: T3, T7 is a ground temperature borehole. The red circle represents the oil pipeline, and CRCOP-II and CRCOP-I are distributed sequentially from west to east.

4.4. ERT and the Cross-Sectional Isotherm Profile for Imaging Permafrost and Talik

Figure 14 depicts the correspondence relationship between the ERT inversion profile and the cross-sectional isotherm profile of Profile 1 of the MDS304 site on 12 April 2018 (a), 6 April 2019 (b), and 18 April 2021 (c). A blue dashed frame depicts the range of coincidence between the ERT inversion profile and the isotherm. The length of the ERT measured section was generally greater than 100 m, and the coverage area included the majority of the Jinsong site's ground temperature monitoring section. In comparison with the cross-sectional isotherm profile (Figures 12 and 13), the ERT profile results have a higher resolution and clearly show the resistivity distribution between T3, T1, T2, T4, T6, and T7 boreholes, thus can distinguish the distribution and variation of permafrost or talik between boreholes. In contrast, the arrangement spacing of the ground temperature monitoring boreholes in Profile 1 appears to be sparse, but the approximate boundary range of the permafrost and talik distribution areas can still be obtained. At the same time,

only the middle position of the ERT profile has the largest depth of the measured strata and an inverted trapezoidal distribution. So, the cross-sectional isotherm profiles have a good supplement to this deficiency of ERT. The combination of the two methods is important for properly understanding the distribution and variation of the underlying permafrost and talik. From the low resistivity area (yellow block) in the ERT inversion profile and the change of 0 °C isotherm in the cross-sectional isotherm profiles (Figure 14), the results show that the permafrost near the pipeline is gradually degrading, and the thermal influence range of surface pond and underlying pipeline gradually forms a connected melting zone.

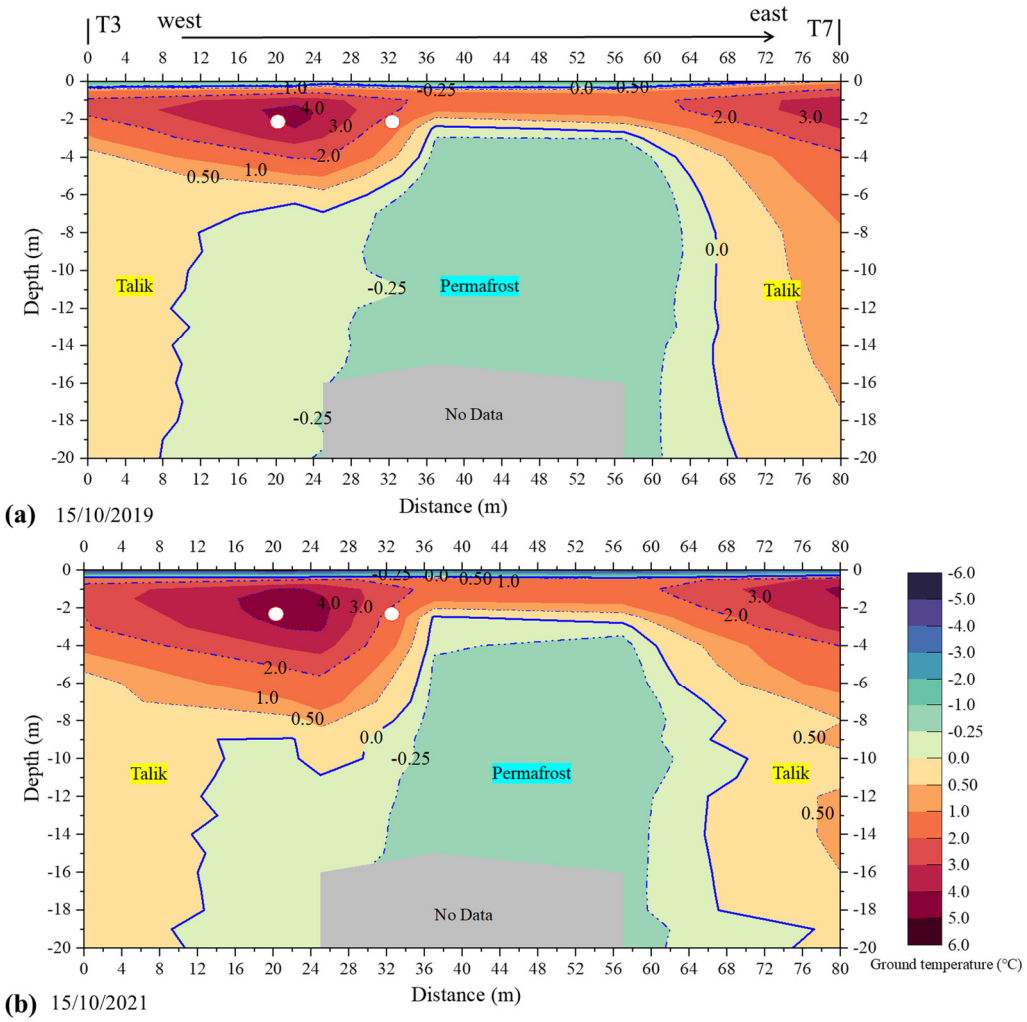

Figure 13. The cross-sectional isotherm profiles of the MDS304 site on 15 October 2019 (**a**) and 15 October 2021 (**b**) were drawn by using the inverse distance weighting method. Note: T3, T7 is a ground temperature borehole. The red circle represents the oil pipeline, and CRCOP-II and CRCOP-I are distributed sequentially from west to east.

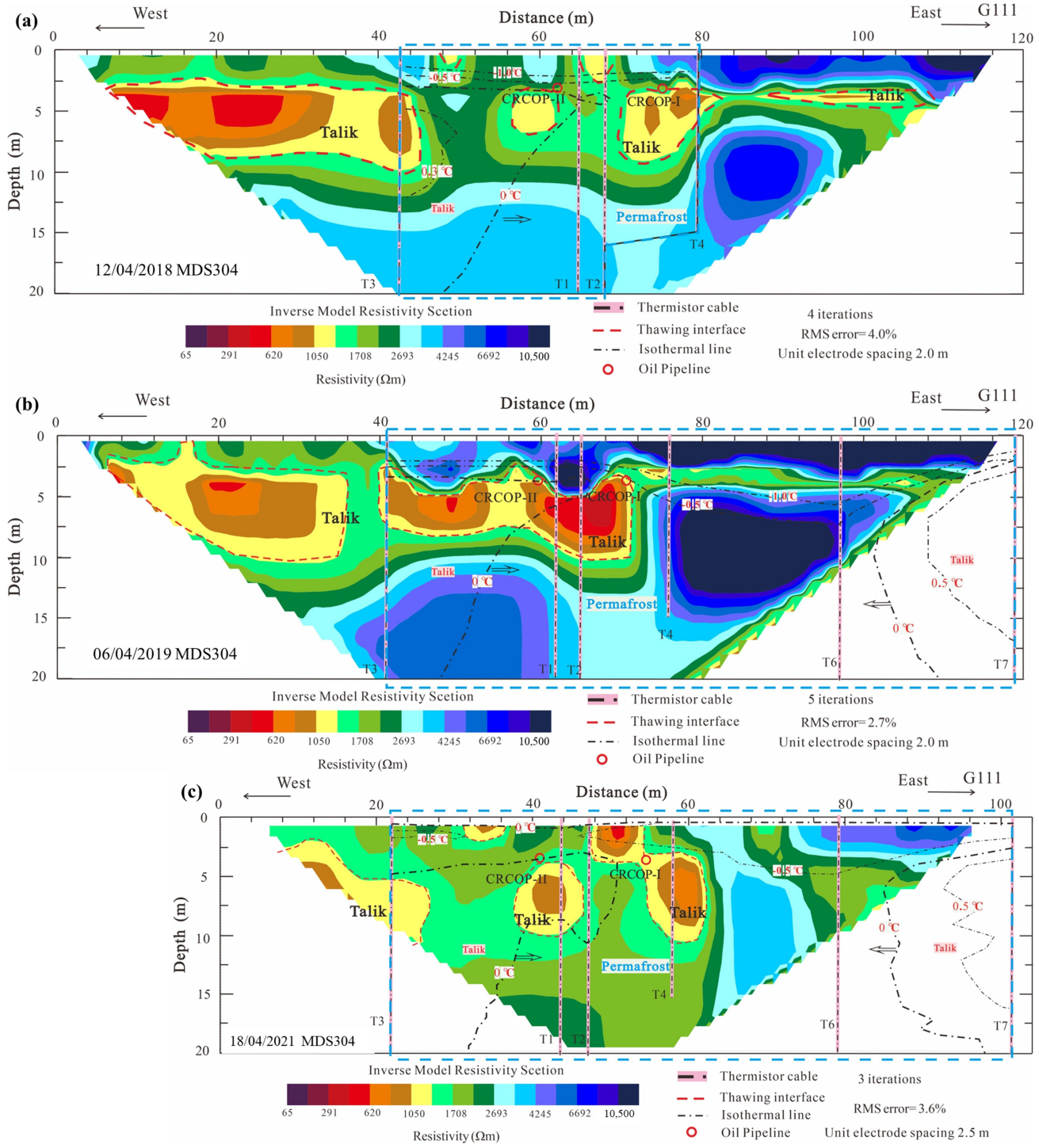

Figure 14. The correspondence between the ERT inversion profile and the cross-sectional isotherm profile of Profile 1 of the MDS304 site on 12 April 2018 (**a**), 6 April 2019 (**b**), and 18 April 2021 (**c**). Note: a blue dashed frame indicates the combination of an ERT inversion profile and an isotherm. T1, . . . , T7 is a ground temperature borehole. The red circle represents the oil pipeline, and CRCOP-II and CRCOP-I are distributed sequentially from west to east.

5. Discussion

The ERT investigation and ground temperature distribution were used in this study to determine the permafrost and talik, active layer thickness, and hydrothermal influence range of pipelines. The accurate distribution range and variation characteristics of permafrost in the study area were obtained by accurate ground temperature monitoring at

multiple point scales combined with continuous resistivity profiling at the surface scale. The results show that the isolated permafrost near the CRCOP at the MDS304 site is degraded in three directions. On the side of the CRCOP's second line, the talik boundary moves about 12 m eastwards from April 2018 to April 2022 at a rate of about 3.0 m/a. The talik boundary between the CRCOP's first line and the G111 highway also moved westward by about 4 m in 2019–2022 at a rate of 1.33 m/a. In addition, the active layer thickness underlying the CRCOP also increased from 6.8 m to 10.8 m in 2019–2021, and the CRCOP's first and second lines experienced settlements of 1.22 m and 1.78 m, respectively. At present, the maximum vertical hydrothermal influence range of the pipelines in the MDS304 site is about 10–12 m (Figure 11). This is consistent with the results of the ERT survey conducted by Li et al. (2021) [37] in typical areas along the CRCOP in August 2019. The ground temperature monitoring of Wang et al. (2019) [43] during 2012–2018 showed that the maximum melting depth at 2 m from the uninsulated pipeline was about 9.8 m, and the maximum melting depth at about 5 m from the insulation pipeline was about 2.21 m. According to our recent ground temperature monitoring results of the MDS304 site, the melting depth at about 5 m from the insulation pipeline increased to about 2.42 m on 15 October 2021 (Figure 15), and the melting depth increased by about 20 cm. In addition, the resistivity of permafrost is affected by many factors, such as lithology, porosity, water content, ice content, and so on [29,30]. At the same time, there are still some uncertainties in the test process of ERT and the interpretation of inversion results, which are mainly affected by the limitation of researchers' professional knowledge and the existence of surface underground ice and ponds on the surface. Our detailed geological data and ground temperature data can reduce the interpretation error of the results. The color block range of the ERT inversion profile corresponding to the 0 °C position in the ground temperature curve, which is used in this study to identify permafrost and talik regions, is similar to previous studies of permafrost distribution in palsa peatland and Southern Yukon [32,33]. Overall, these results demonstrate the effectiveness of ERT and long-term geothermal monitoring in characterizing the distribution and degradation of permafrost in the Da Xing'anling Mountain near the CRCOP.

The result indicates that the permafrost here is facing the risk of widespread degradation. The movement speed of the talik boundary on the side of the CRCOP's second line and the settlement speed of the pipeline exceeds our expectations. There are many factors causing permafrost degradation in the MDS304 site, such as climate warming (Figure 3), warm oil in the pipeline (Figure 8), human engineering activities, lateral thermal erosion of valley rivers, vegetation removal, differential surface settlement and pond thermal erosion (Figure 4). The influence of some factors on permafrost is more obvious on a long-time scale, such as climate warming and warm oil in the pipeline. According to Wang et al. (2018) [8], the pipeline settlement under the influence of oil temperature reached 1.4 m in the Jiagedaqi monitoring section after 4 years of operation. Some factors have a severe influence on permafrost in a short time, such as continuous lateral thermal erosion of the river and pond thermal erosion. Our research results show that the thickness of talik in the permafrost underlying the CRCOP's second line increased by about 6 m under the influence of lateral thermal erosion of the river from 2021 to 2022 (Figure 12). Note that the role of other factors (such as human activities and artificially controlled fire to remove surface vegetation cover) in the long-term degradation of permafrost in this site cannot be obtained from this study, and its quantitative relationship still needs further observation, and research.

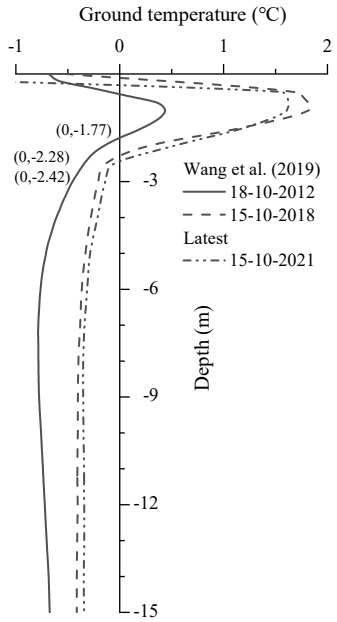

Figure 15. Ground temperature curve of borehole T4 at about 5 m from the insulation pipeline at the MDS304 site, compared with data from Wang et al. (2019) [43].

6. Conclusions

As of 2022, the CRCOP has been in operation for 11 years. This study uses the ERT method in combination with field surveys and ground/oil temperature monitoring to investigate the permafrost degradation at the MDS304 site. The distribution and changes of isolated permafrost and talik were analyzed, and the evolution process of the permafrost near the buried oil pipeline was revealed.

According to oil temperature monitoring results, the monthly average oil temperature at three pumping stations in the permafrost region increased from 10.28–13.84 °C to 10.06–23.78 °C between 2011 and 2020. A rising trend of oil temperature is obvious, which aggravates the degradation of isolated permafrost.

The permafrost area at the MDS304 site is shrinking annually, and the isolated permafrost is degrading in three directions. The ground temperature monitoring results from 2019 to 2021 revealed that the active layer thickness has increased at a rate of 2.0 m/a from about 2.4–6.8 m to 2.5–10.8 m along a cross-section. Meantime, the boundary between permafrost and talik is located near both sides of the CRCOP, and the permafrost is distributed as an island with a length of about 58–60 m, and the mean annual ground temperature is about −0.25 °C.

Permafrost degradation on the side of the CRCOP's second line is more visible due to the river's lateral thermal erosion, where the talik boundary has moved eastward about 12 m during 2018–2022 at a rate of 3.0 m/a. In contrast, the talik boundary between the CRCOP's first line and the G111 highway also moved westward by 4 m in 2019–2022 at a rate of 1.33 m/a. Meanwhile, the maximum displacement of the CRCOP's second line caused by the thawing of frozen soil has reached 1.78 m. These may be related to the differences in topography, vegetation type, peat layer thickness, fire history, and engineering disturbance history. Therefore, decision-makers are recommended to consider the long-term pipeline-permafrost monitoring results in the daily operation and maintenance of the pipeline, which is helpful in taking timely and effective measures to deal with pipeline risks.

Author Contributions: Conceptualization, G.W., G.L., Y.C., F.W., S.Q. and D.C.; methodology, G.W., Y.C., D.C. and G.L.; validation, G.W., G.L., D.C., K.G. and Q.D.; formal analysis, G.W., G.L., D.C., S.Q., X.W. and Q.D.; investigation, G.W., G.L., F.W., Y.C., K.G., X.W., H.J. and Z.Z.; data curation, G.W., Y.C., F.W., X.W., K.G., H.J., Z.Z. and D.C.; writing—original draft preparation, G.W., G.L., Y.C. and

D.C.; writing—review and editing, G.W. and G.L.; visualization, G.W. and S.Q.; supervision, D.C., Y.C., Q.D., S.Q., F.W., X.W., H.J. and Z.Z.; project administration, G.L. and Y.C.; funding acquisition, G.L., D.C. and F.W. All authors have read and agreed to the published version of the manuscript.

Funding: This study was funded by the National Natural Science Foundation of China (Nos. 42272339, 42101121, 42201162) and the Strategic Priority Research Program of the Chinese Academy of Sciences (No. XDA2003020102), and the Research Project of the State Key Laboratory of Frozen Soils Engineering (Grant Nos. SKLFSE-ZY-20, SKLFSE-ZQ-58, SKLFSE-ZT-202203).

Institutional Review Board Statement: Not applicable.

Informed Consent Statement: Not applicable.

Data Availability Statement: Data sharing is not applicable to this article.

Acknowledgments: Many thanks to the geotechnical group of the State Forestry and Grassland Administration's Da Xing'anling Survey and Design Institute, and engineer Guirong Wang of the State Key Laboratory of Frozen soils Engineering, for their assistance in the data collection, field survey, and ERT testing. The authors are very grateful to several anonymous reviewers for their constructive comments and enhanced the early versions of the manuscript.

Conflicts of Interest: The authors declare no conflict of interest.

References

1. IPCC. *Climate Change 2022: Impacts, Adaptation and Vulnerability. Contribution of Working Group II to the Sixth Assessment Report of the Intergovernmental Panel on Climate Change*; Pörtner, H.-O., Roberts, D.C., Tignor, M.M.B., Poloczanska, E.S., Mintenbeck, K., Alegría, A., Craig, M., Langsdorf, S., Löschke, S., Möller, V., et al., Eds.; IPCC: Geneva, Switzerland, 2022; Available online: https://www.ipcc.ch/report/ar6/wg2/ (accessed on 10 July 2022).
2. Chadburn, S.E.; Burke, E.J.; Cox, P.M.; Friedlingstein, P.; Hugelius, G.; Westermann, S. An Observation-Based Constraint on Permafrost Loss as a Function of Global Warming. *Nat. Clim. Change* **2017**, *7*, 340–344. [CrossRef]
3. Jin, H.; Li, S.; Cheng, G.; Shaoling, W.; Li, X. Permafrost and Climatic Change in China. *Glob. Planet Change* **2000**, *26*, 387–404. [CrossRef]
4. Zhang, T. Progress in global permafrost and climate change studies. *Quat. Sci.* **2012**, *32*, 27–38. [CrossRef]
5. Shan, W.; Guo, Y.; Zhang, C. *Understanding the Geological Environmental Risks of Permafrost Degradation-Environmental and Engineering Geology in Permafrost Area in Northeast China*; International Science Council: Paris, France, 2020.
6. Chang, X.; Jin, H.; He, R.; Zhang, Y.; Li, X.; Jin, X.; Li, G. Permafrost Changes in the Northwestern Da Xing'anling Mountains, Northeast China, in the Past Decade. *Earth Syst. Sci. Data.* **2022**, *14*, 3947–3959. [CrossRef]
7. Jin, H.; Yu, Q.; Lü, L.; Guo, D.; He, R.; Yu, S.; Sun, G.; Li, Y. Degradation of Permafrost in the Xing'anling Mountains, Northeastern China. *Permafr. Periglac. Process.* **2007**, *18*, 245–258. [CrossRef]
8. Wang, F.; Li, G.; Ma, W.; Mu, Y.; Zhou, Z.; Mao, Y. Permafrost Thawing along the China-Russia Crude Oil Pipeline and Countermeasures: A Case Study in Jiagedaqi, Northeast China. *Cold Reg. Sci. Technol.* **2018**, *155*, 308–313. [CrossRef]
9. He, R.-X.; Jin, H.-J.; Luo, D.-L.; Li, X.-Y.; Zhou, C.-F.; Jia, N.; Jin, X.-Y.; Li, X.-Y.; Che, T.; Yang, X.; et al. Permafrost Changes in the Nanwenghe Wetlands Reserve on the Southern Slope of the Da Xing'anling—Yile'huli Mountains, Northeast China. *Adv. Clim. Change Res.* **2021**, *12*, 696–709. [CrossRef]
10. Zhang, Z.-Q.; Wu, Q.-B.; Hou, M.-T.; Tai, B.-W.; An, Y.-K. Permafrost Change in Northeast China in the 1950s–2010s. *Adv. Clim. Change Res.* **2021**, *12*, 18–28. [CrossRef]
11. Metz, M.C.; Krzewinski, T.G.; Clarke, E.S. The Trans-Alaska Pipeline System Workpad—An Evaluation of Present Conditions. In *Proceedings Fourth Canadian Permafrost Conference*; National Research Council of Canada: Ottawa, ON, USA, 1982; pp. 523–534.
12. Johnson, E.R. Performance of the Trans-Alaska Oil Pipeline. In *International Conference on Permafrost, 4th, Fairbanks, Alaska, July 17–22, 1983*; Final Proceedings; National Academy Press: Washington, DC, USA, 1984.
13. Burgess, M.; Harry, D. Norman Wells Pipeline Permafrost and Terrain Monitoring: Geothermal and Geomorphic Observations, 1984–1987. *Can. Geotech. J.* **1990**, *27*, 233–244. [CrossRef]
14. Nixon, J.F.; Burgess, M. Norman Wells Pipeline Settlement and Uplift Movements. *Can. Geotech. J.* **1999**, *36*, 119–135. [CrossRef]
15. Yao, Z. Practice and preventive measures for removing ice blockage in Golmud-Lhasa pipeline. *Pipeline Tech. Equip.* **2003**, *1*, 24–27.
16. Huang, S.L.; Bray, M.T.; Akagawa, S.; Fukuda, M. Field Investigation of Soil Heave by a Large Diameter Chilled Gas Pipeline Experiment, Fairbanks, Alaska. *J. Cold Reg. Eng.* **2004**, *18*, 2–34. [CrossRef]
17. He, R.; Jin, H. Permafrost and Cold-Region Environmental Problems of the Oil Product Pipeline from Golmud to Lhasa on the Qinghai–Tibet Plateau and Their Mitigation. *Cold Reg. Sci. Technol.* **2010**, *64*, 279–288. [CrossRef]
18. Li, G.; Ma, W.; Wang, L.; Jin, H.; Wang, Y.; Zhao, Y.; Cai, Y.; Zhang, P. Frost hazards and mitigative measures following operation of Mohe-Daqing line of China-Russia crude oil pipeline. *Rock Soil Mech.* **2015**, *36*, 2963–2973. [CrossRef]

19. Harris, S.A.; Brouchkov, A.; Guodong, C. *Geocryology: Characteristics and Use of Frozen Ground and Permafrost Landforms*; CRC Press: London, 2017; ISBN 978-1-315-16698-8.
20. Jin, H.; Yu, W.; Chen, Y.; Gao, X.; Li, F.; Yao, Z. (Differential) Frost heave and thaw settlement in the engineering design and construction of oil pipelines in Permafrost Regions: A review. *J. Glaciol. Geocryol.* **2005**, *27*, 454–464.
21. Shur, Y.L.; Jorgenson, M.T. Patterns of Permafrost Formation and Degradation in Relation to Climate and Ecosystems. *Permafr. Periglac.* **2007**, *18*, 7–19. [CrossRef]
22. Jorgenson, M.T.; Harden, J.; Kanevskiy, M.; O'Donnell, J.; Wickland, K.; Ewing, S.; Manies, K.; Zhuang, Q.; Shur, Y.; Striegl, R.; et al. Reorganization of Vegetation, Hydrology and Soil Carbon after Permafrost Degradation across Heterogeneous Boreal Landscapes. *Environ. Res. Lett.* **2013**, *8*, 035017. [CrossRef]
23. Osterkamp, T.E.; Romanovsky, V.E. Evidence for Warming and Thawing of Discontinuous Permafrost in Alaska. *Permafr. Periglac. Processes* **1999**, *10*, 17–37. [CrossRef]
24. Panda, S.K.; Prakash, A.; Jorgenson, M.T.; Solie, D.N. Near-Surface Permafrost Distribution Mapping Using Logistic Regression and Remote Sensing in Interior Alaska. *GIScience Remote Sens.* **2012**, *49*, 346–363. [CrossRef]
25. Douglas, T.A.; Jorgenson, M.T.; Brown, D.R.N.; Campbell, S.W.; Hiemstra, C.A.; Saari, S.P.; Bjella, K.; Liljedahl, A.K. Degrading Permafrost Mapped with Electrical Resistivity Tomography, Airborne Imagery and LiDAR, and Seasonal Thaw Measurements. *Geophysics* **2016**, *81*, WA71–WA85. [CrossRef]
26. Li, X.; Jin, H.; He, R.; Huang, Y.; Wang, H.; Luo, D.; Jin, X.; Lü, L.; Wang, L.; Li, W.; et al. Effects of Forest Fires on the Permafrost Environment in the Northern Da Xing'anling (Hinggan) Mountains, Northeast China. *Permafr. Periglac. Processes* **2019**, *30*, 163–177. [CrossRef]
27. Guo, Y.; Shan, W.; Xu, Z.; Wang, C.; Wang, S. Identification Old Landslides in Permafrost Degradation Area in Northeast China by Difference Distribution of Surface Trees. In *Understanding and Reducing Landslide Disaster Risk*; ICL Contribution to Landslide Disaster Risk Reduction; Vilímek, V., Wang, F., Strom, A., Sassa, K., Bobrowsky, P.T., Takara, K., Eds.; Springer: Cham, Switzerland, 2021; pp. 275–281. ISBN 978-3-030-60318-2.
28. Jin, X.; Jin, H.; Iwahana, G.; Marchenko, S.S.; Luo, D.; Li, X.; Liang, S. Impacts of Climate-Induced Permafrost Degradation on Vegetation: A Review. *Adv. Clim. Change Res.* **2021**, *12*, 29–47. [CrossRef]
29. Hauck, C.; Kneisel, C. Applied Geophysics in Periglacial Environments. In *Applied Geophysics in Periglacial Environments*; Cambridge University Press: Cambridge, UK, 2008; pp. 1–240. ISBN 978-0-521-88966-7.
30. Hauck, C. New Concepts in Geophysical Surveying and Data Interpretation for Permafrost Terrain. *Permafr. Periglac. Processes* **2013**, *24*, 131–137. [CrossRef]
31. Harada, K.; Yoshikawa, K. Permafrost Age and Thickness near Adventfjorden, Spitsbergen. *Polar Geogr.* **1996**, *20*, 267–281. [CrossRef]
32. Sjöberg, Y.; Marklund, P.; Pettersson, R.; Lyon, S.W. Geophysical Mapping of Palsa Peatland Permafrost. *Cryosphere* **2015**, *9*, 465–478. [CrossRef]
33. Lewkowicz, A.G.; Etzelmüller, B.; Smith, S.L. Characteristics of Discontinuous Permafrost Based on Ground Temperature Measurements and Electrical Resistivity Tomography, Southern Yukon, Canada. *Permafr. Periglac. Processes* **2011**, *22*, 320–342. [CrossRef]
34. Hubbard, S.S.; Gangodagamage, C.; Dafflon, B.; Wainwright, H.; Peterson, J.; Gusmeroli, A.; Ulrich, C.; Wu, Y.; Wilson, C.; Rowland, J.; et al. Quantifying and Relating Land-Surface and Subsurface Variability in Permafrost Environments Using LiDAR and Surface Geophysical Datasets. *Hydrogeol. J.* **2013**, *21*, 149–169. [CrossRef]
35. You, Y.; Yu, Q.; Pan, X.; Wang, X.; Guo, L. Geophysical Imaging of Permafrost and Talik Configuration Beneath a Thermokarst Lake: Imaging Permafrost and Talik of a Thermokarst Lake. *Permafrost Periglac.* **2017**, *28*, 470–476. [CrossRef]
36. Duvillard, P.-A.; Magnin, F.; Revil, A.; Legay, A.; Ravanel, L.; Abdulsamad, F.; Coperey, A. Temperature Distribution in a Permafrost-Affected Rock Ridge from Conductivity and Induced Polarization Tomography. *Geophys. J. Int.* **2021**, *225*, 1207–1221. [CrossRef]
37. Li, X.; Jin, X.; Wang, X.; Jin, H.; Tang, L.; Li, X.; He, R.; Li, Y.; Huang, C.; Zhang, S. Investigation of Permafrost Engineering Geological Environment with Electrical Resistivity Tomography: A Case Study along the China-Russia Crude Oil Pipelines. *Eng. Geol.* **2021**, *291*, 106237. [CrossRef]
38. Wang, Y.; Jin, H.; Li, G. Investigation of the Freeze–Thaw States of Foundation Soils in Permafrost Areas along the China–Russia Crude Oil Pipeline (CRCOP) Route Using Ground-Penetrating Radar (GPR). *Cold Reg. Sci. Technol.* **2016**, *126*, 10–21. [CrossRef]
39. Jin, H.; Hao, J.; Chang, X.; Zhang, J.; Yu, Q.; Qi, J.; Lü, L.; Wang, S. Zonation and Assessment of Frozen-Ground Conditions for Engineering Geology along the China–Russia Crude Oil Pipeline Route from Mo'he to Daqing, Northeastern China. *Cold Reg. Sci. Technol.* **2010**, *64*, 213–225. [CrossRef]
40. Chang, X.; Jin, H.; He, R.; Jing, H.; Li, G.; Wang, Y.; Luo, D.; Yu, S.; Sun, H. Review of permafrost monitoring in the northern Da Hinggan Mountains, Northeast China. *J. Glaciol. Geocryol.* **2013**, *35*, 93–100. [CrossRef]
41. Li, G.; Wang, F.; Ma, W.; Fortier, R.; Mu, Y.; Zhou, Z.; Mao, Y.; Cai, Y. Field Observations of Cooling Performance of Thermosyphons on Permafrost under the China-Russia Crude Oil Pipeline. *Appl. Therm. Eng.* **2018**, *141*, 688–696. [CrossRef]
42. Wang, F.; Li, G.; Ma, W.; Wu, Q.; Serban, M.; Vera, S.; Alexandr, F.; Jiang, N.; Wang, B. Pipeline–Permafrost Interaction Monitoring System along the China–Russia Crude Oil Pipeline. *Eng. Geol.* **2019**, *254*, 113–125. [CrossRef]

43. Wang, F.; Li, G.; Ma, W.; Mao, Y.; Mu, Y.; Serban, M.; Cai, Y. Permafrost Warming along the Mo'he-Jiagedaqi Section of the China-Russia Crude Oil Pipeline. *J. Mt. Sci.* **2019**, *16*, 285–295. [CrossRef]
44. Zhou, Y.; Guo, D.; Qiu, G.; Cheng, G.; Li, S. *Geocryology in China*; Science Press: Beijing, China, 2000; pp. 170–194.
45. Wei, Z.; Jin, H.; Zhang, J.; Yu, S.; Han, X.; Ji, Y.; He, R.; Chang, X. Prediction of Permafrost Changes in Northeastern China under a Changing Climate. *Sci. China Earth Sci.* **2011**, *54*, 924–935. [CrossRef]
46. Jin, H.; Sun, G.; Yu, S.; Jin, R.; He, R. Symbiosis of Marshes and Permafrost in Da and Xiao Hinggan Mountains in Northeastern China. *Chin. Geogr. Sci.* **2008**, *18*, 62–69. [CrossRef]
47. Chang, X.; Jin, H.; Zhang, Y.; Sun, H. Study of seasonal snow cover influencing the ground thermal regime on western flank of Da Xing'anling Mountains, northeastern China. *Sci. Cold Arid Reg.* **2015**, *7*, 666–674.
48. Jin, H.; Yu, S.; Lv, L.; Guo, D.; Li, Y. Degradation of permafrost in the Da and Xiao Hinggn Mountains, Northeast China, and preliminary assessment of its trend. *J. Glaciol. Geocryol.* **2006**, *28*, 467–476.
49. Wang, Y.; Jin, H.; Hao, J.-Q.; Li, G.; Cai, Y.; He, S. Pipe-Laying Technology in a Subarctic Permafrost Region: A Case Study for the China-Russia Crude Oil Pipeline from Mo' He to Daqing, Northern Northeast China. In Proceedings of the 68th Canadian Geotechnical Conference and 7th Canadian Permafrost Conference, Quebec, QC, Canada, 20–23 September 2015.
50. You, Y.; Yu, Q.; Pan, X.; Wang, X.; Guo, L. Application of Electrical Resistivity Tomography in Investigating Depth of Permafrost Base and Permafrost Structure in Tibetan Plateau. *Cold Reg. Sci. Technol.* **2013**, *87*, 19–26. [CrossRef]
51. Li, G.; Ma, W.; Wang, F.; Jin, H.; Alexander, F.; Chen, D.; Wu, G.; Cao, Y.; Zhou, Y.; Mu, Y.; et al. A Newly Integrated Ground Temperature Dataset of Permafrost along the China-Russia Crude Oil Pipeline Route in Northeast China. *Earth Syst. Sci. Data Discuss.* **2022**, *14*, 5093–5110. [CrossRef]
52. Li, G.; Sheng, Y.; Jin, H.; Ma, W.; Qi, J.; Wen, Z.; Zhang, B.; Mu, Y.; Bi, G. Forecasting the Oil Temperatures along the Proposed China–Russia Crude Oil Pipeline Using Quasi 3-D Transient Heat Conduction Model. *Cold Reg. Sci. Technol.* **2010**, *64*, 235–242. [CrossRef]
53. Dahlin, T.; Zhou, B. A Numerical Comparison of 2D Resistivity Imaging with 10 Electrode Arrays. *Geophys. Prospect.* **2004**, *52*, 379–398. [CrossRef]
54. Liu, H.; Niu, F.; Niu, Y.; Xu, J.; Wang, T. Effect of Structures and Sunny–Shady Slopes on Thermal Characteristics of Subgrade along the Harbin–Dalian Passenger Dedicated Line in Northeast China. *Cold Reg. Sci. Technol.* **2016**, *123*, 14–21. [CrossRef]
55. Hilbich, C.; Marescot, L.; Hauck, C.; Loke, M.H.; Mäusbacher, R. Applicability of Electrical Resistivity Tomography Monitoring to Coarse Blocky and Ice-Rich Permafrost Landforms. *Permafr. Periglac.* **2009**, *20*, 269–284. [CrossRef]
56. Grifka, J.; Weigand, M.; Kemna, A.; Heinze, T. Impact of an Uncertain Structural Constraint on Electrical Resistivity Tomography for Water Content Estimation in Landslides. *Land* **2022**, *11*, 1207. [CrossRef]
57. Hauck, C.; Mühll, D.V. Inversion and Interpretation of Two-Dimensional Geoelectrical Measurements for Detecting Permafrost in Mountainous Regions. *Permafr. Periglac. Processes* **2003**, *14*, 305–318. [CrossRef]
58. Loke, M.H.; Acworth, I.; Dahlin, T. A Comparison of Smooth and Blocky Inversion Methods in 2D Electrical Imaging Surveys. *Explor. Geophys.* **2003**, *34*, 182–187. [CrossRef]
59. Olayinka, A.I.; Yaramanci, U. Use of Block Inversion in the 2-D Interpretation of Apparent Resistivity Data and Its Comparison with Smooth Inversion. *J. Appl. Geophys.* **2000**, *45*, 63–81. [CrossRef]
60. Smith, T.; Hoversten, M.; Gasperikova, E.; Morrison, F. Sharp Boundary Inversion of 2D Magnetotelluric Data. *Geophys. Prospect.* **1999**, *47*, 469–486. [CrossRef]
61. Forte, E.; French, H.M.; Raffi, R.; Santin, I.; Guglielmin, M. Investigations of Polygonal Patterned Ground in Continuous Antarctic Permafrost by Means of Ground Penetrating Radar and Electrical Resistivity Tomography: Some Unexpected Correlations. *Permafr. Periglac. Processes* **2022**, *33*, 226–240. [CrossRef]
62. Cao, Y.; Li, G.; Wu, G.; Chen, D.; Gao, K.; Tang, L.; Jia, H.; Che, F. Proposal of a New Method for Controlling the Thaw of Permafrost around the China–Russia Crude Oil Pipeline and a Preliminary Study of Its Ventilation Capacity. *Water* **2021**, *13*, 2908. [CrossRef]
63. Mu, Y.; Li, G.; Wei, M.; Zhengmin, S.; Zhou, Z.; Wang, F. Rapid Permafrost Thaw Induced by Heat Loss from a Buried Warm-Oil Pipeline and a New Mitigation Measure Combining Seasonal Air-Cooled Embankment and Pipe Insulation. *Energy* **2020**, *203*, 117919. [CrossRef]
64. Yoshikawa, K.; Bolton, W.R.; Romanovsky, V.E.; Fukuda, M.; Hinzman, L.D. Impacts of Wildfire on the Permafrost in the Boreal Forests of Interior Alaska. *J. Geophys. Res.* **2002**, *108*, 8148. [CrossRef]
65. Wendler, G.; Conner, J.; Moore, B.; Shulski, M.; Stuefer, M. Climatology of Alaskan Wildfires with Special Emphasis on the Extreme Year of 2004. *Theor. Appl. Climatol.* **2011**, *104*, 459–472. [CrossRef]
66. Brown, D.R.N.; Jorgenson, M.T.; Douglas, T.A.; Romanovsky, V.E.; Kielland, K.; Hiemstra, C.; Euskirchen, E.S.; Ruess, R.W. Interactive Effects of Wildfire and Climate on Permafrost Degradation in Alaskan Lowland Forests. *J. Geophys. Res. Biogeosciences* **2015**, *120*, 1619–1637. [CrossRef]
67. Chai, M.T.; Mu, Y.H.; Li, G.Y.; Ma, W.; Wang, F. Relationship between ponding and topographic factors along the China-Russia Crude Oil Pipeline in permafrost regions. *Sci. Cold Arid Reg.* **2019**, *11*, 419–427.

68. Chai, M.; Li, G.; Wei, M.; Cao, Y.; Gang, W.; Mu, Y.; Chen, D.; Jun, Z.; Zhou, Z.; Yu, Z.; et al. Assessment of Freeze-Thaw Hazards and Water Features along the China-Russia Crude Oil Pipeline in Permafrost Regions. *Remote Sens.* **2020**, *12*, 3576. [CrossRef]
69. Mu, Y.; Chai, M. Thermal influence of ponding and buried warm-oil pipelines on permafrost: A case study of the China-Russia Crude Oil Pipeline. *Sci. Cold Arid Reg.* **2020**, *12*, 59–70. [CrossRef]